A structural investigation of erbium titanate and lanthanum tungstate by CBED

Fredrik Sydow Hage

Department of Physics
University of Oslo

Thesis is submitted in partial fulfillment
of the requirements for the degree of

Master of Science in Materials, Energy and Nanotechnology

June 2nd 2009

Preface

This thesis is submitted to the Department of Physics, University of Oslo in partial fulfillment of the requirements for the degree of Master of Science in Materials, Energy and Nanotechnology. The work was done at FERMiO (Funtional EnergyRelated Materials in Oslo) and the Department of Physics, Univeristy of Oslo, during the period august 2007 to june 2009.

Fredrik Sydow Hage

Oslo, June 2nd 2009.

Abstract

A previous electron diffraction study during a student project indicated that $Er_{1.96}Ca_{0.04}Ti_2O_{6.98}$ exhibit a primitive Bravais lattice. This result has not been repeated during the current investigations. The same TEM specimen as used during the student project was reinvestigated as well as new samples prepared by both a dry- and a wet method of synthesis. $Er_{1.96}Ca_{0.04}Ti_2O_{6.98}$ has been determined to exhibit a face centered cubic Bravais lattice and to crystallize in the Fd3m (no. 227) space group by SAD and CBED. This is in accordance with the reported space group for $Er_2Ti_2O_7$. None of the following factors have been found to affect the Bravais lattice of the structure: doping with divalent calcium ions, holmium impurities, phase transitions, order- disorder transitions of defects, water content and the method of synthesis. No explanation has been found for the inconsistency in exhibited Bravais lattice.

Lanthanum tungstate with a nominal La/W ratio of 5.6 was studies by electron diffraction. Samples were prepared by the freeze-drying method. CBED patterns indicated that the compound crystallize in a quasi- Fd3m space group. However SAD patterns indicated a primitive cubic lattice where the d- glide plain symmetry breaks down. Magrasó et al. have reported that this compound crystallizes in the F-43m space group by XRD and NPD. CBED, SAD and XRD/NPD results are in disagreement, which might be explained by small range structural disorder, but this warrants further investigation.

Contents

Figures

Tables

Equations

Chapter 1

Introduction

An increasing demand for energy is currently one of humanity's biggest challenges. The world population is expected to increase significantly and as a result of this, the demand for energy will grow. The current energy supply has severe byproducts such as air pollution, acid precipitation, ozone depletion, forest destruction, and emission of radioactive substances as well as a relation to global warming. Hence there is a need for cleaner and more self sustainable methods of supplying energy.

Fuel cells are promising as clean energy converters. A fuel cell converts chemical energy to electric energy and heat directly from a fuel gas without an intermediate combustion reaction. This direct energy conversion gives rise to a much higher efficiency than obtained by conventional thermo- mechanical methods. Efficiency is dependent on the fuel which is typically hydrogen, methanol or hydrocarbons. Solid oxide fuel cells (SOFSs) promise to be very useful for large, high- power applications such as large scale industrial stations and electricity- generating power stations. SOFCs are operated at 600-1000 ºC and are therefore labeled as high temperature fuel cells. Their efficiency can reach up to 70 % (and an additional 20 % with heat recovery). A SOFC consists of a ceramic electrolyte (such as yttria- stabilized zirconia) sandwiched between two ceramic electrodes. Physical and chemical properties such as conductivity and stability of the components are crucial to the functionality of a SOFC. Electrolyte materials exhibit pure ionic conductivity while electrode materials exhibit mixed proton- electron conductivity Challenges for SOFCs today consists of finding materials with high conductivity which also exhibit high chemical stability and compatibility, high strength, low cost and fabricability (Stambouli and Traversa 2002).

Materials exhibiting high ionic conductivity may also be of interest for sensors. This might be done by applying a voltage over a high temperature proton conductor in contact with a probed system and a reference system. Materials with high mixed proton- electron conduction are also of interest for gas- separation membranes (i.e. hydrogen, oxygen and carbon dioxide). In hydrogen separation membranes, high hydrogen conductivity allows for efficient and selective transport of hydrogen. The necessary electron countercurrent exhibited by the same material allows for the transport process to occur without an

external circuit or electrodes (Norby 1998). It is important to determine the structure of such materials to be able to fully understand and explain their properties. The scope of this work has been to determine the structure two such oxide materials. These structures have been described by crystallography. The key principles of crystallography will be presented in the following sections.

1.1 An introduction to crystallography

Materials with a periodic arrangement of atoms are referred to as crystalline while materials with a random arrangement of atoms are referred to as amorphous. An area of a continuous repeated arrangement is refereed to as a crystal. The ordering of a crystal is referred to as its structure, which can be described by specifying a repeating element and its translational periodicity. A mathematically derived lattice can be used as a reference for the atomic positions in a crystal structure and the repeating element can be replaced by a lattice point. All lattice points have the same atomic environment and are often associated with several atoms. The smallest building block of a lattice is called a unit cell which can be specified by three basis vectors a, b and c and the angles between them α, β and γ, see table 1.1. The lattice can be generated by translations along these vectors, see equation 1.1 where u, v and w are integers.

[1.1] $t = u\,a + v\,b + w\,c$

Atomic positions within a unit cell can be described by a vector r. The coordinates of an atom position is then given by (x, y, z), see equation 1.2.

[1.2] $r = x\,a + y\,b + z\,c$

Table 1.1: The axial systems (Olsen 2008).

Axial system	Axes	Interaxial angles
Triclinic	$a \neq b \neq c$	$\alpha \neq \beta \neq \gamma \neq 90°$
Monoclinic	$a \neq b \neq c$	$\alpha = \gamma = 90° \neq \beta$
Orthorhombic	$a \neq b \neq c$	$\alpha = \beta = \gamma = 90°$
Tetragonal	$a = b \neq c$	$\alpha = \beta = \gamma = 90°$
Cubic	$a = b = c$	$\alpha = \beta = \gamma = 90°$
Hexagonal	$a_1 = a_2 = a_3 \neq c$	$\alpha = \beta = 90°$ $\gamma = 120°$
Rhombohedral	$a = b = c$	$\alpha = \beta = \gamma \neq 90°$

1.1.1 Miller indices

The Miller indexing system is commonly used for representing directions and planes in crystals. A crystal is described by an axial system defined by the basis vectors of the unit cell. The Miller indices of a plane (hkl) are given from the reciprocal intercepts of the plane on these axes (a/h, b/k, c/l). Miller indices are usually scaled so that all are integers and as small as possible. If a lattice plane is parallel to one or more of the basis vectors, the corresponding Miller indices are zero and if a plane intersects on the negative axis of origin, the corresponding indices are negative. All parallel lattice planes have the same indices in this system due to the translational properties of the lattice. Directions in crystals are described by the Miller indices [uvw] of the translational vector, t, of the lattice system, see equation 1.1. A vector in the required direction is constrained to pass through the origin of the axial system. For hexagonal crystals four indices are used (hkil) where $i = - (h + k)$. The general notation of Millers indices are:

(hkl) means a single set of parallel lattice plains
{hkl} mean equivalent planes , i.e. (110) and (101) in a cubic crystal
[uvw] means a single zone axis or direction
<uvw> means directions of equivalent type

The lattice plane spacing, d, is given by the relation $d_{hkl} = 1/ |g_{hkl}|$, where $|g_{hkl}|$ is the length of the reciprocal space lattice vector, see equation 1.3:

[1.3] $g_{hkl} = h\ a^* + k\ b^* + l\ c^*$.

Where a* = (b x c) / V, b* = (c x a) / V, and c* = (a x b) / V

V is the unit cell volume. For crystals with orthogonal axes: V = a • (b x c) = b • (c x a) = c • (a x b).

1.1.2 Bravais lattice

There are innumerous possible lattice bases. In crystallography, classification is based on 14 three- dimensional Bravais lattices, which only takes translational properties into account. A Bravais lattice can be described by a combination of on crystal system (Triclinic, Monoclinic, Orthorhombic, Tetragonal, Hexagonal, Trigonal or Cubic) and lattice centering (primitive (P), face centered (F), body centered (I), rombohedral (R) or bace centered (A, B, C)). Base centered lattice centered lattices are given symbols A, B or C if there are lattice point on the a, b or c face. The above mentioned symbols for lattice centering (i.e. F, I and P) are called Hermann- Mauguin symbols (Olsen 2008). The 14 Bravais are listed in table 1.2.

Table 1.2: The 14 Bravais lattices (Olsen 2008).

Crystal system	Bravais lattice	Herman- Mauguin symbol
Triclinic	Primitive	P
Monoclinic	Primitive	P
	Base- centered*	A, B or C
Orthorhombic	Primitive	P
	Base- centered*	A, B or C
	Face- centered	F
	Body- centered	I
Tetragonal	Primitive	P
	Body- centered	I
Hexagonal	Primitive	P†
Trigonal	Primitive	
	Rhombohedral	R
Cubic	Primitive	P
	Face- centered	F
	Body- centered	I

* The symbol for base centering A, B or C corresponds to the a-, b- or c- face where the lattice point is situated.
† This Bravais lattice can be described by both the hexagonal and trigonal crystal system.

1.1.3 Point group

Crystal structures can also be classified by a group of symmetry operations which all leave at least on point unmoved, and thus do not include translational operations. Such point groups consist of the macroscopic symmetry elements: rotational axes (1, 2, 3, 4 and 6), mirror plane (m) and rotations- inversion axes (-1, -2, -3, -4 and -6). The -1 rotation- inversion axis is also called the center of symmetry. There are 32 distinct three dimensional crystallographic point groups which have been derived from possible combinations of macroscopic symmetry elements.

1.1.4 Space group

In addition to the macroscopic symmetry elements crystals can have two microscopic symmetry elements which involve translation within a unit cell. These can be glide plains (a, b, c, n or d) and screw axes (2, 2_1, 3, 3_1, 3_2, 4, 4_1, 4_2, 4_3, 6, 6_1, 6_2, 6_3, 6_4 and 6_5). If all translational properties and all symmetry elements are combined, crystals can be classified in 230 space groups (Olsen 2008). For example the Fd3m space group (no. 227) which consists of a face centered cubic lattice, the m3m point group and a d glide plane. Details about crystal description by space groups are given in International Tables of Crystallography (Hahn 1983).

1.1.5 Wyckoff positions

Atomic positions of a space group are often referred to by Wyckoff positions which are related to so-called (crystallographic point) orbits. The set of symmetry equivalent sites in a space group is referred to as an orbit. A Wyckoff position is equivalent to a corresponding orbit if the coordinates of a site are completely fixed by symmetry (i.e. ½, ½, ½). However if the site includes one or more freely variable coordinates (i.e. x in x, 0, ½) the Wyckoff position corresponds to an infinite amount of possible orbits, there are one orbit per value of the variable. For example, the set of sites symmetrically equivalent to i.e. 0.1, 0, ½ make up one orbit and the set symmetrically equivalent to 0.12, 0, ½, makes up one orbit but they both belong to the same Wyckoff position. Wyckoff position notation is given by the multiplicity (determining the number of atoms that can be accommodated on the given position) and a letter a, b, …h (from the highest to lowest

degree of symmetry). For example the denomination 4c designates the four symmetry equivalent points to an orbit c within the unit cell. A shift of space group origin induces a cyclic permutation of Wyckoff positions and thereby a change in the Wyckoff letters (Müller 2006).

1.2 Transmission Electron Microscope (TEM)

The theoretical limit of resolution in a microscope is in the order of magnitude of the wavelength of the illumination. Therefore, the resolution limit set by visible light is far surpassed by that of the electron. An electron microscope shares some basic features of the optical microscope, but is much more complex in design.

The transmission electron microscope consists of an electron gun, a system of magnetic lenses, a phosphorescent viewing screen, detectors and a film compartment. The electrons are emitted from a filament and accelerated towards an anode by a high negative electrical potential (80– 1000 kV). The electrons originate from a filament which is either a tungsten hairpin or a LaB_6 crystal or from a field emission source. The magnetic field produced by the lenses is axial but strongly inhomogeneous and result in a spiral electron trajectory which constant pitch. All magnetic lenses of the microscope are converging, which means that the electron trajectory is centered at the optical axis.

A wide array of signals is produced when the electron beam interacts with a thin specimen. The signals mainly utilized in TEM are transmitted electrons, diffracted electrons and characteristic x- rays.

There are two main modes of operating a TEM; the *image mode* and the *diffraction mode*. In *image mode*, all electrons originating from one point in the specimen are imaged onto one point in the *image plane*, see figure 1.1. In *diffraction mode* all electrons which are scattered at the same angle by the specimen are imaged onto a point in the *diffraction plane* (also called the *back focal plane*), see figure 1.6. The mode of operation is chosen by changing the current, thus the strength, of the magnetic lenses. Both the image- and the diffraction plane can be recorded by a photographic film which is placed in a compartment under the viewing screen.
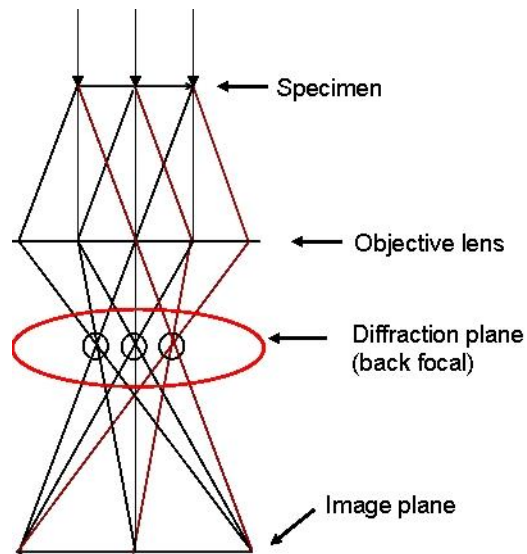
Figure 1.1: The ray path of the electron beam in TEM (image mode). The diffraction (back focal) plane is indicated.

The JEOL JEM 2000FX is an analytic transmission electron microscope which was used in the present study. It was equipped with a LaB_6 filament and operated at an acceleration voltage of 200kV ($\lambda = 0.0251$ Å). An EDS system was attached and data refinement was done by the Noran System Six (NSS) software. Elements of $Z \geq 5$ may be detected. The 2000FX was operated with a Gatan $\pm 25°$ double tilt cooling specimen holder. The point to point resolution specified by JEOL is 0.3 nm.

1.2.1 Electron Diffraction (ED)

Electrons are charged and scattered therefore strongly by the nucleuses and the electrons of a material through Coulomb forces. Thus electron diffraction is very sensitive to changes in the crystal structure (i.e. antiphase boundaries, dislocations, strain and stacking faults) and the spatial resolution of a TEM makes it possible to analyze nanometer sizes areas by ED.

Electrons undergo both kinematical and dynamical scattering. Kinematical scattering is described in more detail in section 1.2.2. Dynamical scattering contributes substantially

to the resulting diffraction pattern (DP). This must be taken into consideration when interpreting an electron DP. An important dynamical effect is called multiple diffraction or multiple scattering, which results in that kinematically forbidden reflections are observed in a DP. This is caused by that each scattering direction can be considered as the direction of the incident beam for new scattering events. Such reflections may be observed in DPs of multiphase materials or when several crystals are arranged along the beam incidence. Reflections which are kinematically forbidden due to glide planes and screw axes might also be observed in DPs from single crystals due to double scattering. An example of this is the 002- type reflections observed in the electron diffraction patterns of Si which are kinematically forbidden due to the d glide plane of the Fd3m space group. Due to dynamical effects it is also difficult to get reliable kinematical intensities of reflections from ED.

1.2.2 Selected Area Diffraction (SAD)

Electrons will scatter when passing through a sample. They scatter kinematically according to Bragg's law:

[1.4] $2d \sin (\theta_B) = n\lambda$

d : The lattice plane distance
n: An integer
λ: The wavelength of the incident radiation (in this case electrons)
θ_B: The angle between the incident beam and the Bragg reflection.
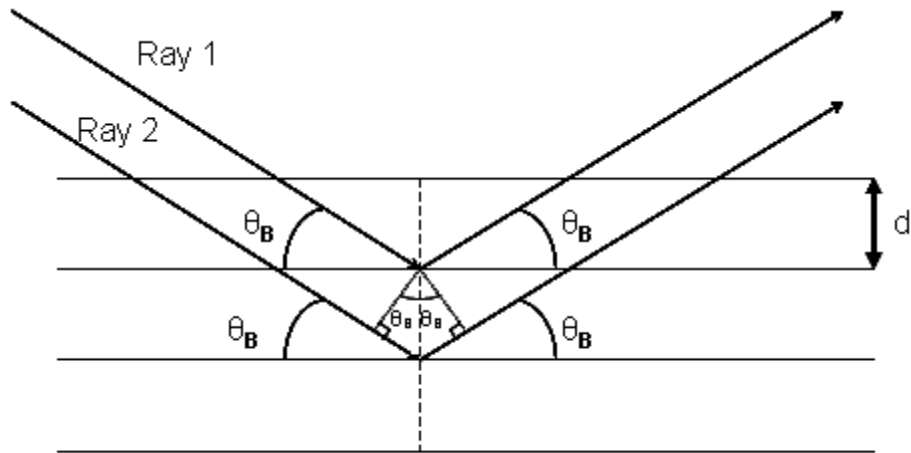
Figure 1.2: Illustration of Bragg scattering of lattice planes. Path difference between ray 1 and ray 2 is: $n \lambda = 2d \sin (\theta_B)$.

The lattice spacing, d, is related to the Bragg scattering angle, θ_B. The measured distance between the observed Bragg reflection and the central beam is $R = 2 \tan(2\theta_B)$, as seen in figure 1.3. L is the camera length (the effective distance between the specimen and the observed diffraction pattern). The scattering angle is small in TEM. It can therefore be approximated that:

[1.5] $R = L (\lambda/d)$.

Then:

[1.6] $R d = L \lambda = K \leftrightarrow d = L (\lambda/R) = K/R$

K is called the camera constant. This relates the lattice spacing directly to a radius, R, of a reflection in the diffraction pattern (DP).
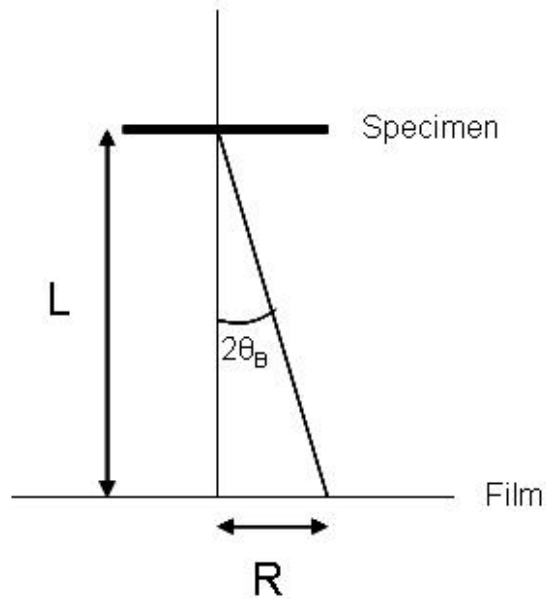
Figure 1.3: Illustration of the principal geometric relation between the camera length L, the radius R and the Bragg scattering angle θ_B.

Electrons scattered from a specific area of the sample can be selected by inserting an aperture into the image plane. The diffraction technique which utilizes such an aperture and a parallel electron beam illumination is called selected area diffraction (SAD). The observed DP can be regarded as a two dimensional projection of reciprocal space normal to the incident beam (Williams and Carter 1996; Olsen 2008). A typical analysis area in SAD is 0.5 μm^2.

1.2.3 Calibrating the JEOL JEM 2000FX

Calibration of the camera constant of the TEM instrument is necessary to improve the accuracy of the d- values measured from electron diffraction patterns. All SAD patterns in this study were obtained at eucentric height. The calibration was done by using a silicon specimen as a standard, since silicon is a well studied material. Silicon crystallizes in the Fd3m (no. 227) space group with a lattice size parameter of a = 5.43029(4) Å and with Si placed at the 8a Wyckoff position (Straumanis, et al. 1961). The JEM 2000FX has a nominal accelerating voltage of 200kV. A silicon specimen was prepared from a wafer by the crushing method, see section 1.2.6.1. The R values of the [110] and [110] projections were measured for a nominal camera lengths of 66 cm and of 130 cm. These R values were multiplied by the corresponding d- values reported for Si. Mean camera constants were calculated from all measured R values, see equation 1.6. They were found

to be 1.533 ± 0.006 Å cm and 3.52 ± 0.03 Å cm respectively. This corresponds to camera lengths of 61.08 cm and 140 cm, when assuming that the nominal electron wavelength of 0.0251 Å (E = 200keV) is the actual wavelength of the electrons in the microscope.

1.2.4 Convergent Beam Electron Diffraction (CBED)

In SAD, the incidence of the electron beam is parallel and normal to the specimen surface. When the electron beam is converged onto the specimen, the resulting image of the diffraction plane is called a Convergent Beam Electron Diffraction (CBED) pattern. The converged electron beam interacts with several "layers" in reciprocal space called "Laue Zones", see figure 1.4. CBED therefore contains three-dimensional crystallographic information about the specimen. The Laue Zones are labeled: zero order Laue zone (ZOLZ), first order Laue zone (FOLZ), second order Laue Zone (SOLZ) and so on. Laue zones of a higher order than zero is collectively named higher order Laue zones (HOLZ). In CBED patterns, HOLZ are observed as rings with the ZOLZ at its center. The diameter of a HOLZ ring is related to the lattice size parameter as described in literature. The three- dimensional information available in CBED patterns makes it possible to determine specimen properties such as crystallographic point group, -space group, lattice size parameter, thickness and defects/ dislocations (Williams and Carter 1996).

A relatively large area is illuminated by a parallel electron beam in SAD, while the area illuminated in CBED is determined by the probe formed by the converged beam. Therefore the information obtained from CBED has a higher degree of spatial accuracy than that of SAD. Typical areas of analysis of both ED techniques are indicated in figure 1.5.

Due to the convergence of the beam, the sharp "spot- reflections" observed in SAD expand to discs, see figure 1.6. The diameter of these discs is determined by the convergence semi-angle, see equation 1.7.

[1.7] $\alpha = (r_1/r)\ (\lambda/d)$.

d: Lattice plane distance.

λ: Electron wavelength.

r_1: Measured radius of reflection disc.

r: Measured distance from the 000 reflection (central beam) to the hkl (Bragg) reflection.

This angle is controlled by 2nd condenser aperture and the current of the 2nd condenser lens. When α is small, reflection-discs do not overlap, which results in a Kossel-Möllenstedt pattern, see figure 3.4. When α is large, there is an overlap of reflection discs which results in a Kossel pattern (Williams and Carter 1996), see figure 1.4.
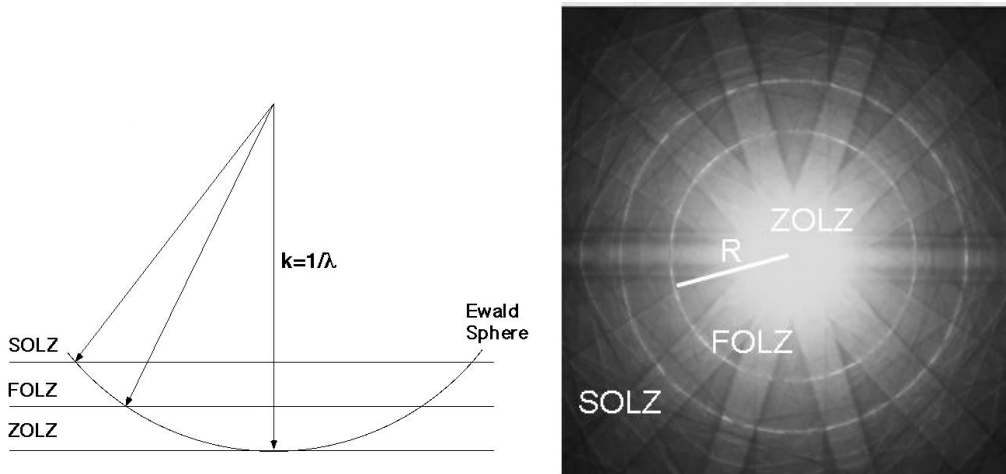
Figure 1.4: Illustration of the formation of HOLZ rings in CBED (left). Kossel CBED pattern, the ZOLZ, FOLZ and SOLZ are indicated (right).
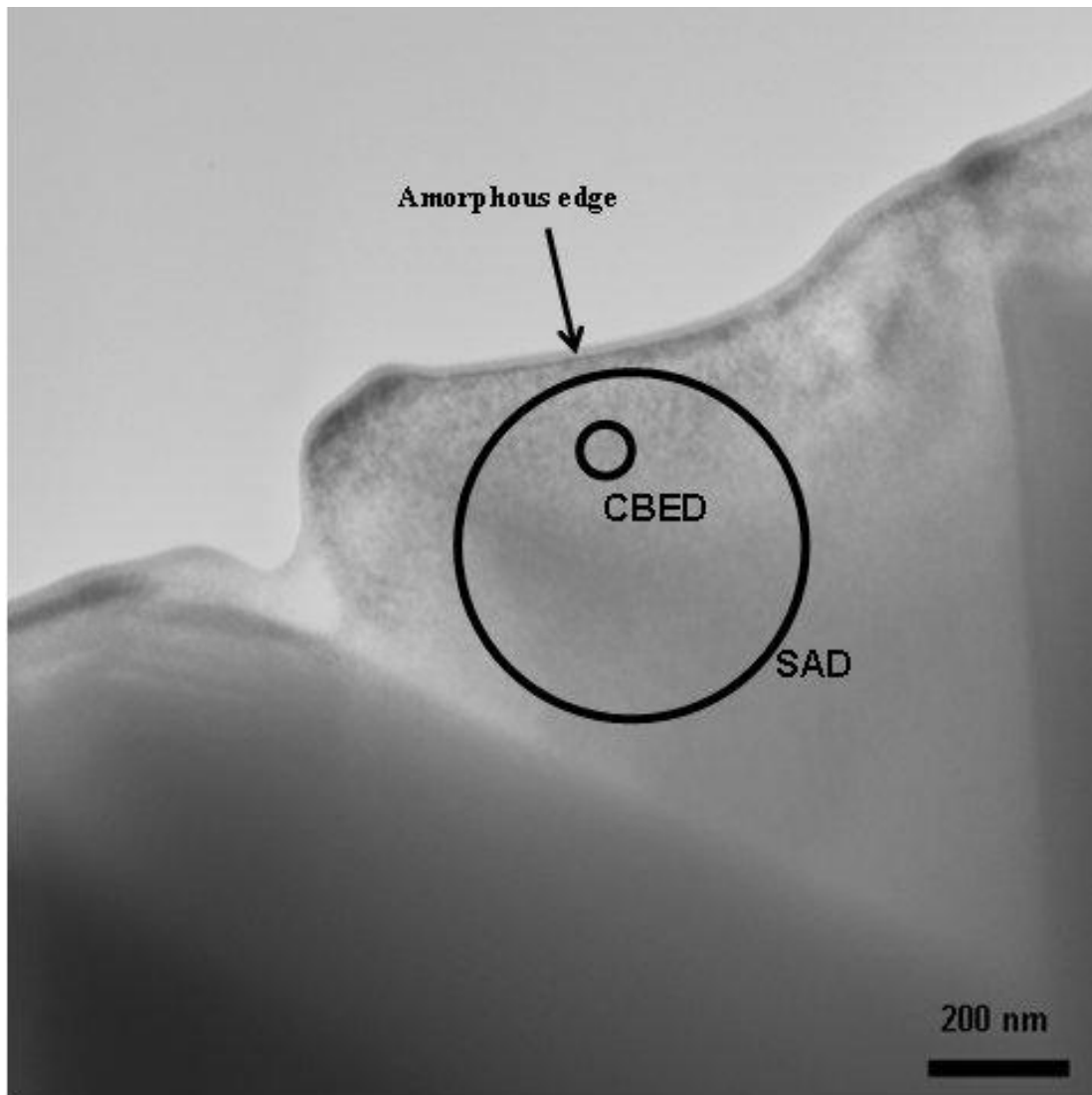
Figure 1.5: Typical size of areas investigated by CBED and SAD. This is a TEM image of a single lanthanum tungstate crystal at [100] beam incidence.
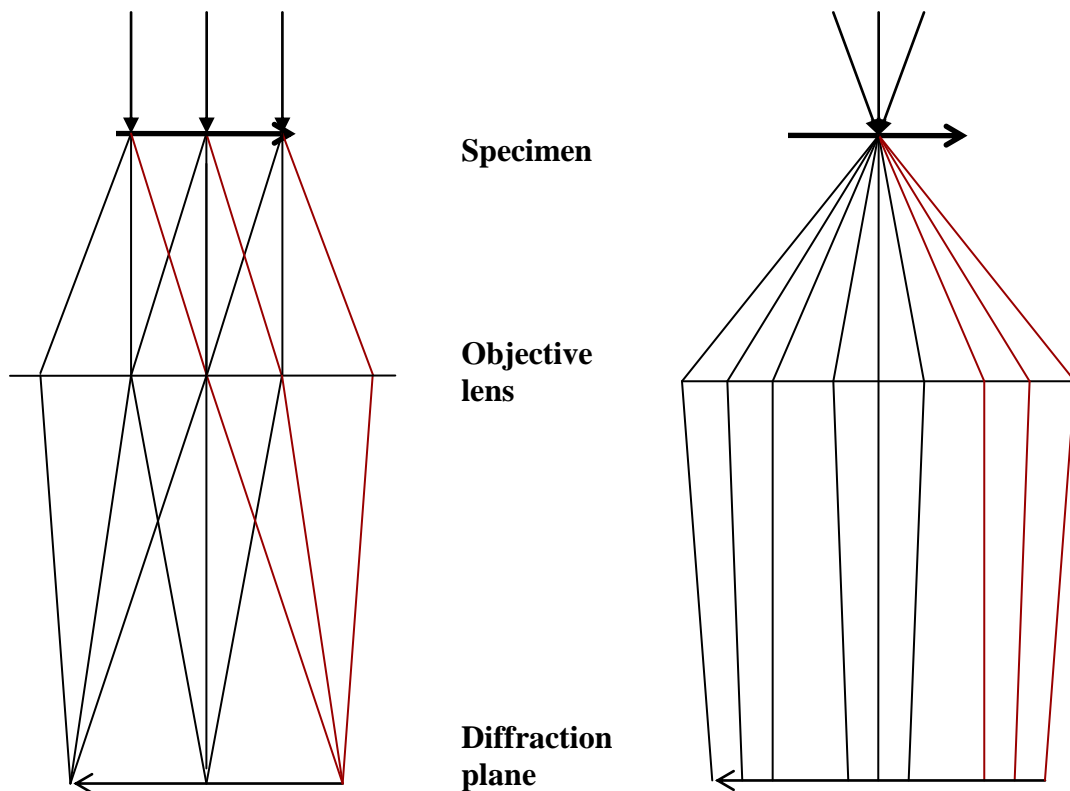
Figure 1.6: Ray diagrams for SAD (left) and CBED (right).

1.2.4.1 Point group

The crystallographic point group of the specimen can be determined from one or more CBED zone axis patterns. CBED pattern symmetry is related to point groups by diffraction groups. Symmetry elements which can be observed in CBED patterns are: 1, 2, 3, 4, 6, m, 2mm, 3m, 4mm or 6mm.

The symmetry of a pattern at a small camera length (L < 1m), which can include higher order Laue Zones (HOLZ), is called whole pattern (WP) symmetry. The bright field (BF) symmetry is the symmetry of the HOLZ lines within the 000 disc of the direct non- Bragg scattered beam. HOLZ lines are caused by three-dimensional interactions. When only diffuse two-dimensional intensity is observed, the symmetry is referred to as BF projection symmetry. WP symmetry is often sufficient to determine the point group so

obtaining the BF symmetry is usually not critical. The WP symmetry is always equal to- or lower than the BF symmetry. (Buxton et al. 1976; Steeds and Vincent 1983; Tanaka et al. 1983, 1) Possible WP and BF symmetries and their corresponding diffraction groups are given in table 1.3. Diffraction groups and their corresponding point groups are given in table 1.4.

Table 1.3: The relation between observed BF and WP symmetries and possible diffraction groups (Buxton et al. 1976).

diffraction group	bright field	whole pattern
1	1	1
1_R	2	1
2	2	2
2_R	1	1
21_R	2	2
m_R	m	1
m	m	m
$m1_R$	2mm	m
$2m_Rm_R$	2mm	2
2mm	2mm	2mm
2_Rmm_R	m	m
$2mm1_R$	2mm	2mm
4	4	4
4_R	4	2
41_R	4	4
$4m_Rm_R$	4mm	4
4mm	4mm	4mm
4_Rmm_R	4mm	2mm
$4mm1_R$	4mm	4mm
3	3	3
31_R	6	3
$3m_R$	3m	3
3m	3m	3m
$3m1_R$	6mm	3m
6	6	6
6_R	3	3
61_R	6	6
$6m_Rm_R$	6mm	6
6mm	6mm	6mm
6_Rmm_R	3m	3m
$6mm1_R$	6mm	6mm

Table 1.4: The derivation of possible point groups by diffraction groups (Buxton et al. 1976).

1.2.4.2 Space group

A space group can be determined when the translational symmetry elements are added to the point group and Bravais lattice. Possible translational symmetry elements are glide planes (a, b, c, n and d) and screw axis (2, 2_1, 3, 3_1, 3_2, 4, 4_1, 4_2, 4_3, 6, 6_1, 6_2, 6_3, 6_4 and 6_5).

Translational symmetry operations can be projected onto CBED patterns. This manifests itself as Gjønnes- Moodie (GM) lines in the reflection discs. GM lines are dynamical extinction lines appearing in a CBED disc when this reflection is caused by dynamical- rather than kinematical (Bragg) electron scattering. Lines caused by a glide plane are

called A- lines and lines caused by screw axis are called B- lines. An A line is parallel to the reflection disc g- vector while a B- line is perpendicular to it. A- and B-lines can be caused by two- or three dimensional interactions. If the line is broad, it is regarded as caused by two-dimensional interactions and is denoted A_2 or B_2. If a line or a set for lines are thin, they are regarded as caused by three-dimensional interactions and are denoted as A_3 or B_3. When both lines caused by two- and three-dimensional interactions are present, the broad A_2 or B_2 lines tend to mask the weaker A_3 or B_3 lines (Gjonnes and Moodie 1965; Steeds and Vincent 1983; Tanaka et al. 1983, 2).

When the electron beam is parallel to the surface of the specimen, the reflections discs are reduced to spots and the dynamical extinction lines are no longer observable. This is why kinematically forbidden reflections can be observed in SAD patterns while still being in congruence with the selection rules for the space group. The intensities of these forbidden reflections are expected to decrease as the DP is tilted of zone axis (Williams and Carter 1996).

1.2.5 Energy Dispersive Spectroscopy (EDS)

Energy dispersive x-ray spectroscopy (EDXS, EDX or EDS) utilizes the characteristic x-rays produced by the electron beam interaction with the specimen. When an incident electron excites a core level electron of an atom in the specimen, one of two relaxation processes may occur: Auger electron emission or the emission of characteristic x-rays. Auger electrons are ejected from the atom as a result of a recombination- relaxation process. Theses electrons are utilized in Auger electron spectroscopy and x-ray photoelectron spectroscopy (XPS). The characteristic x- rays are emitted when the excited electron "falls down" to its original state and the residual energy difference is disposed of as an x-ray photon (usually 1- 20 eV). The energy of the emitted photon is determined by the energy levels which are characteristic of the element from which it originates.

The X-rays are detected by a liquid nitrogen cooled solid state detector, (usually a Li doped Si crystal). The mass concentration of two elements C_i and C_j are related to so called Cliff- Lorimer factors k_{ij} by:

[1.8] $C_i / C_j = k_{ij} (I_i / I_j)$.

I_i and I_j are the intensities of the x-ray signals. This relation is used for quantitative x-ray analysis. These k- factors are independent of specimen thickness if the specimen is thin. The TEM specimens are thin, and therefore there is no need to take fluorescence and absorption into account (Olsen 2008).

1.2.6 TEM specimen preparation

There exist several different specimen preparation techniques for TEM. In the present study, two preparation techniques were chosen: crushing and ion milling.

The crushing technique is simple and fast but results in small analyzable areas. The technique involving mechanical grinding and ion milling produces high quality samples with large analyzable areas. The drawback of this technique is that it is time consuming and the specimen might be damaged by Ar^+ ion beam heating. Both methods were used in the present study to determine if heating by the ion beam had a significant effect on the crystal structure of the sample.

1.2.6.1 Crushing

The sample material was crushed in an agate mortar with ethanol or isopropanol until the mixture was slurry-like. Some of the slurry (containing fine particles) is gathered by a pipette and a droplet is placed on a holey carbon amorphous film supported by a cupper grid. The solvent evaporates in room temperature leaving the fine particles glued to the film. Some of the edges of the particles should now be thin enough to be transparent to electrons.

1.2.6.2 Mechanical thinning and ion milling

A circular specimen with a diameter of 3mm was cut by an Ultrasonic Disc Cutter (Gatan Model 601), and was then mechanically ground by SiC paper and polished. The specimen was then glued to a cupper ring for mechanical support and ion milled (Gatan Model 691, Precision ion polishing system) until a hole appeared. The Cu ring used was 3mm in diameter with a central slot of 1 mm x 2 mm. Subsequently to ion milling, the edge of the hole should be thin enough to be electron transparent, typically less than ~200 nm.

A Gatan model 656 Dimple Grinder was also was used for mechanical thinning. A dimpler creates a "dimple" at the center of the specimen in stead of thinning it uniformly. This results in a higher mechanical stability of the specimen due to thicker edges. The specimen was glued to a glass rod with crystal bind and placed at the center of a rotating table. A rotating dimpling wheel was placed on top of the specimen. A paste with 3-6 μm SiC particles and a few droplets of ethanol were applied to the dimpling wheel. After the dimpling, the sample was glued to a cupper ring of 3 mm diameter and ion milled.

Mechanical grinding with subsequent ion milling is a time consuming technique, but yields a larger and more uniform area for analysis than the crushing technique. An amorphous edge will often appear due to breakdown of the crystalline order from heating by the ion beam. This should be taken into consideration during analysis. The effect of heating can be reduced by decreasing the energy of the ions and the angle of ion beam incidence.

1.3 Scanning Electron Microscope (SEM)

The scanning electron microscope utilizes, as TEM, electrons as illumination. The electron beam is generated by an electron gun. The electrons originate from a filament which is either a tungsten hairpin or a LaB_6 crystal or from a field emission source. The electrons are focused by a set of magnetic lenses and rastered over the sample by a set of electrostatic coils. The accelerating voltage utilized in SEM range typically from 0.5 kV to 30 kV. The resolution limit in SEM is in the order of 2 nm. SEM is a surface technique. Electrons are detected as they escape the surface of the sample and are scattered back towards the electron beam. The main signals detected in SEM are secondary electrons, backscattered electrons and characteristic x- rays.

Secondary electrons (SE) (E < 50 eV) are produced by inelastic scattering and contain topographical information. They are collected by an Everhart- Thornley detector. SE electrons have a relative low energy so they can have a hard time reaching the detector on their own. A biased grid is therefore placed in front of the ET- detector to accelerate the electrons towards it.

Backscattered electrons (BSE) are produced by elastic (or nearly elastic) scattering and contain atomic element information (Z- contrast). They are detected by two solid state detectors placed right beside the electron gun. The penetration depth of the electron beam is related to the density of the sample. Electrons will not penetrate as deep into high Z elements as low Z elements. Therefore a higher amount of electrons will be scattered back towards the detector for high Z elements than lower Z elements. This results in that an area containing higher Z elements will appear brighter than lower z elements. It is therefore possible to distinguish between areas containing different compositions of elements by BSE. However, this technique does not yield any information about which elements actually are present. The signals from both detectors can be combined by a computer to form an image containing both topography and Z- contrast.

I the present study a FEI Quanta 200F scanning electron microscope was used. It was equipped with a field emission electron gun (FEG) and a EDAX EDS detector. The microscope was operated at low vacuum mode ($1x10^{-3}$ Pa) to avoid charging of the sample. The porosity of the sample surface was of interest so no sample preparation such as polishing or chemical etching was required. The samples were simply fastened to the holders by a carbon tape. The microscope was operated at an acceleration voltage of 15kV.

1.3.1 EDS in SEM

The principle of EDS is the same in SEM as in TEM: characteristic x-rays are detected after they leave the sample. The intensity of the characteristic x-rays yields information about which elements are present and an approximate composition of the investigated area. The typical minimal obtainable area of analysis for EDS in SEM is about 1 μm^3. This limit is set by the x-ray interaction volume. By combining BSE and EDS

information, the identification of different phases should be possible if phase domains are larger than ~1 μm^3.

1.4 X- Ray Diffraction (XRD)

X- ray diffraction is based on Bragg scattering of crystallographic planes, as in electron diffraction (ED), see 1.2.2. The major differences between XRD and ED are the way the radiation interacts with the sample and the size of the area which is investigated of a specimen. Nanometer sized areas can investigated by electron diffraction in TEM, while the collected diffraction data from XRD originates from a large bulk sample. Hence the structural description obtained by XRD reflects the mean structure. X-rays are mainly scattered kinematically in a sample. Thus kinematical intensities and lattice size parameters can be obtained with high accuracy in XRD.

Sample preparation was done by adding a few droplets of ethanol to a small amount of crushed sample. This slurry- like mixture was distributed evenly as a thin layer onto a glass plate. The ethanol evaporated and left an evenly distributed layer of sample material on the glass plate. The glass is amorphous which does not contribute sharp Bragg reflections in the resulting diffractogram.

The X- ray diffraction experiments were done on a Siemens D-5000 diffractometer located at the Department of Chemistry at the University of Oslo. The diffractometer was configured with a Bragg- Brentano geometry and a Cu Kα_1 radiation of wavelength λ = 1.5406 Å. Cu Kα_1 and Cu Kα_2 (λ = 1.5444 Å) are separated spatially by Bragg scattering from a Ge crystal (different wavelengths equals different scattering angles). The function of the Ge crystal is therefore as a monochromator. A single slit is then used to stop the Cu Kα_2 from reaching the surface.

The XRD diffraction data was analyzed by the EVA 8.0.0.2. software developed by SOCABIM. The degree of phase purity was determined by comparing XRD data from the PDFMaintEx library 8.0.113. from $Er_2Ti_2O_7$, Er_2O_3 and TiO_2 to the observed data. The detection limit is typically ~1-2 wt%, but is in practice highly dependent on experimental conditions. Theoretical calculations of intensities and plane distances of $Er_{1.96}Ca_{0.04}Ti_2O_{6.98}$ were done by the ATOMS 5.1 software developed by Eric Dowty

(2000). Lattice plane calculations of lanthanum tungstate were done by the PowderCell 2.4 software developed by W. Kraus and G. Nolze.

Chapter 2

Erbium titanate

$Er_2Ti_2O_7$ is an oxygen ion conductor (Tuller 1994). Doping of stoichiometric pyrochloric rare earth titanates by divalent calcium ions is found to increase the ionic conductivity by an increase of free mobile charge carriers (Kramer et al. 1994).

$Er_{1.96}Ca_{0.04}Ti_2O_{6.98}$ exhibits predominantly oxygen ion conduction in grain interiors, while protons have been found to play an important role as charge carriers in boundary related processes (Fjeld et al. 2008). Some possible applications for $Er_2Ti_2O_7$ or related materials are high temperature electrolytes and electrodes (Subramanian 1993). Such components are crucial in the development of effective fuel cells and gas separation membranes.

In april 2007 $Er_{1.96}Ca_{0.04}Ti_2O_{6.98}$ was examined during a student project by TEM (Vigen and Ertzied 2007). SAD patterns were indexed in agreement with a cubic primitive unit cell with size parameter a = 10.0762(6) Å reported for $Er_2Ti_2O_7$ (Knop et al. 1965). Indexed SAD patterns of the [100] and [110] projections are shown in figure 2.1. The strong reflections in the [100] projection are the 00l and 0kk reflections, where k, l = 4n. The strong reflections in the [110] projection are the 00l and hhh reflections where h = 2n and l = 4n. The weak reflections observed in both SAD patterns can not be indexed in accordance with the face centered cubic Bravais lattice reported for $Er_2Ti_2O_7$ (Knop et al. 1965). To the knowledge of the author there are no reports of the structure of the Ca^{2+} doped compound. It was therefore interesting to investigate the structure of this compound and what might have caused this apparent change in Bravais lattice.
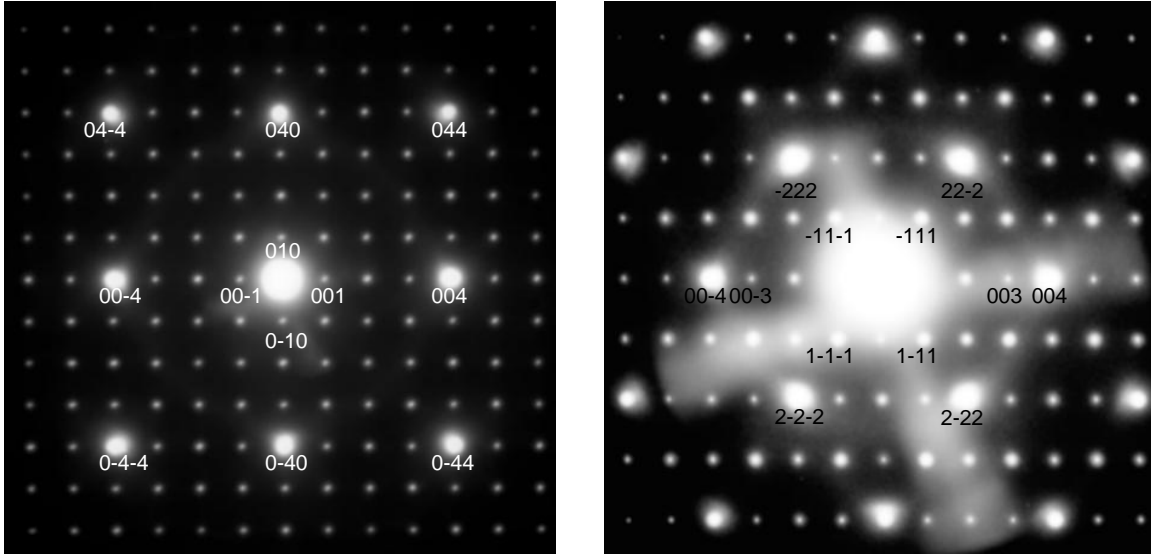
Figure 2.1: SAD patterns of the [100] projection (left) and the [110] projection (right). The strong reflections in the [100] projection are the 00l and 0kk reflections, where k, l = 4n. The strong reflections in the [110] projection are the 00l and hhh reflections where h = 2n and l = 4n.

2.1 Pyrochlore structured erbium titanate

The pyrochlore structure is named after the mineral pyrochlorite $(NaCa)(NbTa)O_6/(OH)$. Over 450 synthetic substances are known to crystallize in the pyrochlore structure (Subramanian et al. 1983; Chakoumakos 1984). The oxide pyrochlores have an ideal formula of $A_2B_2O^1_6O^2$, (where A and B are cations and O^1 and O^2 are oxygen ions occupying different independent crystallographical sites). Compounds with non-ideal formulas, such as $A_2B_2O_6$ and AB_2O_6, does also crystallize in the pyrochlore structure, and are regarded as defect pyrochlores. More complex combinations of elements do also occur, where the A or B element is partially substituted by other cations of other valence charges (Subramanian et al. 1983; Lian et al. 2003).

The A- element can be a rare earth or an element with lone-pair electrons and the B-element can be a transitional metal with a variable oxidation state or a post transitional metal. In addition, the structure tolerates substitutions and vacancies. This result in a variety of physical properties exhibited within this group. For instance, the electrical nature of pyrochlores ranges from highly insulating through semi conducting to metallic.

This leads to possible applications such as oxygen conductors, oxygen sensors, proton conductors, and solar energy converters (Subramanian et al. 1983) and play a role in radioactive waste disposal (Lian et al. 2003)

2.1.1 Crystallography

The space group of the ideal oxide pyrochlore structure is Fd3m (no. 227), where eight molecular units occupy each unit cell. There are four crystallographically independent sites in this structure: A, B, O^1 and O^2, all of which can be chosen as origin. The A- and B cations are in addition at inversion centers for the structure. In literature, the most common choice of origin is the B site, Wyckoff position 16c. According to this description the A cation is situated at 16d (½, ½, ½) and the oxygens O^1 and O^2 are situated at 48f (x, 1/8, 1/8) and 8b (3/8, 3/8, 3/8) respectively. This description is given in table 2.1.

Table 2.1: The positions of the ideal oxide pyrochlore structure, B chosen as origin (Subramanian et al. 1983).

Atom	Position (Wyckoff)	Coordinates	Occupancy
A	16d	½, ½, ½	1
B	16c	0, 0, 0	1
O^1	48f	x, 1/8, 1/8	1
O^2	8b	3/8, 3/8, 3/8	1

There are two parameters that determine this structure: the x- positional parameter of the O^1 oxygen at the 48f site and the lattice size parameter (Subramanian et al. 1983). These parameters have been determined experimentally by refining data from x-ray diffraction (Brixner 1964; Knop et al. 1965), neutron diffraction (Knop et al. 1965; Knop et al. 1969) and electron diffraction (Tabira et al. 2000), and by theoretical computer simulations (Minervini et al. 2002) for many oxide pyrochlore compounds.

2.1.2 Description of the pyrochlore structure

In literature, the pyrochlore structure is usually described as a distorted and disordered fluorite- type structure (Subramanian et al. 1983; Wilde and Catlow 1998; Lian et al. 2003).

The fluorite structure is named after CaF_2. MX_2 is the general formula for this structure, where the M is a metal cation and the X is an anion. Bonding in this structure is usually of a strongly ionic character due to the relatively high difference in electronegativity between the species. The M cations are ordered in a face centered cubic lattice and the X ions occupy the tetrahedral interstitial sites (Subramanian et al. 1983).

In the pyrochlore structure, the A and B cations are situated at the M sites of the fluorite structure. The A and B cations are ordered in alternate [110] rows in every other (001) plane and in alternate [-110] rows in the other (001) planes.

This arrangement of cations results in three different interstices for anions:

- 48f position (x, 1/8, 1/8): two A and two B as nearest neighbors
- 8a position (1/8, 1/8, 1/8): four B cations as nearest neighbors
- 8b position (3/8, 3/8, 3/8): four A cations as nearest neighbors

The 8a positions (1/8, 1/8, 1/8) are vacant in the ideal pyrochlore structure, see figure 2.2. This results in a tendency of electrostatic shielding of the B cations from each other by a displacement of the anions at the 48f site. These anions are "pulled" from the center of its tetrahedral interstices (x=0.375) towards its two neighboring B cations (x= 0.3125). At x=0.3125 the 48f anions are in a perfect octahedral environment of B ions that share

corners in the [110] direction (Subramanian et al. 1983). An illustration of the effect of the x- parameter on coordination can be seen in figure 2.3. This distortions changes the B- O^1-B angle from 109 ° 28´ to 132°, while the O^2 anions remains at the same distance from its neighboring A cations.

Vacant 8a sites

Vacant 8a sites
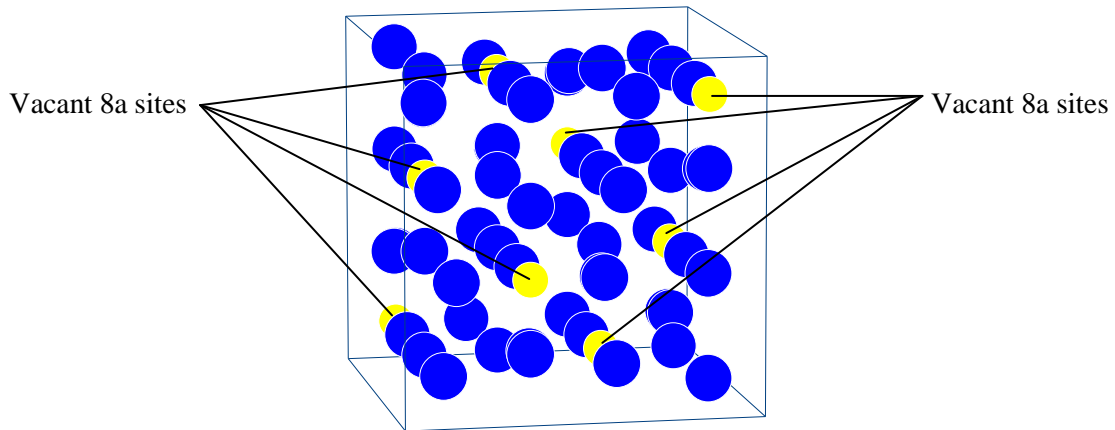
Figure 2.2: The oxygen atoms of the pyrochlore structure indicted by blue spheres. Vacancies at the 8a positions (1/8, 1/8, 1/8) (Subramanian et al. 1983) are indicated in by yellow spheres. Figure was made by PowderCell 2.4.

(a)

x = 0.3125

- B (16c)
- A (16d)
- O (48f)
- O´(8b)

(b)

x = 0.375
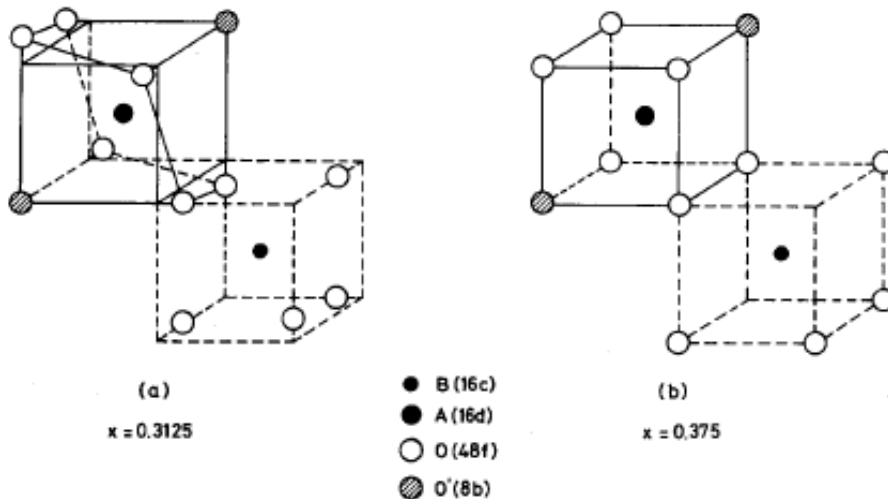
Figure 2.3: The effect on the coordination polyhedron around the cations for the two extreme values of the 48f x- parameter. (O= O^1, O´ = O^2) (Subramanian et al. 1983)

2.1.3 $Er_2Ti_2O_7$

In a study by Knop et al., different arrangements of the atoms in erbium titanate were discussed based on the refinement of data from neutron- and x-ray diffraction. The most probable atomic arrangement for this compound was found to be that of the pyrochlore structure (Knop et al. 1965). This result has later been found by refinement of x-ray diffraction data (Lau et al. 2006) as seen in table 2.2. The partial occupancy of Er on 16c and Ti on 16d is due to cation anti- site pair as described by equation 2.1. $Er_2Ti_2O_7$ is oxygen ion conducting (Tuller 1994), not UV fluorescent in the visible spectrum and exhibit p-type semi conductance at elevated temperatures (Brixner 1964).

Table 2.2: The positions of the $Er_2Ti_2O_7$ pyrochlore structure refined from X-ray diffraction data. Ti is chosen as origin (Lau et al. 2006). The partial occupancy of Er on 16c and Ti on 16d is due to cation anti- site disorder as described by equation 2.1.

Atom	Position (Wyckoff)	Coordinates	Occupancy
Er	16d	½, ½, ½	0.969(2)
	16c	0, 0, 0	0.031(2)
Ti	16c	0, 0, 0	0.969(2)
	16d	½, ½, ½	0.031(2)
O^1	48f	0.3283(5), 1/8, 1/8	1
O^2	8b	3/8, 3/8, 3/8	1
	8a	1/8, 1/8, 1/8	0

In literature, poly crystalline samples are most commonly achieved by dry mixing of Er_2O_3- and TiO_2 powders which is then pressed into tablets. The tablets are subsequently heated repeatedly at temperatures, T: 1000 ºC$\leq$ T$\leq$1500 ºC. (Brixner 1964; Knop et al. 1965; Tabira et al. 2000; Lau et al. 2006). Knop et al. reports that $Er_2Ti_2O_7$ crystallize directly in the pyrochlore phase after dry-mixing and heating of stoichiometric amounts of Er_2O_3 and TiO_2 at 1100 ºC. This conclusion is reached after the x-ray data revealed no sign of the intermediate Er_2TiO_5, which is formed for other rare- earth pyrochlore titanates (Knop et al. 1969).

An alternative to the dry-mix synthesis is precipitation. A mixture of a nitric- or hydrochloric acid solution of Er_2O_3 and an aqueous solution of $TiCl_4$ are treated with aqueous ammonia. The product is filtered off, washed with water and dried at 100 ℃ (Shcherbakova et al. 1979).

Single crystals have been grown from a molten mixture of Er_2O_3, TiO_2 and PbF_2 at T= 1508 K. This synthesis requires slow evaporation of PbF_2 during a five-day high temperature synthesis period. Excess PbF_2, mainly on the surface, was removed mechanically (Lian et al. 2003).

There is a good agreement on the value of lattice size parameter. Minor differences in the reported lattice size parameter are accredited to slight differences in synthesis and methods of data refinement (Lian et al. 2003). Reported values for the lattice size parameter and the x- positional parameter of the O^1 oxygen (at the 48f site) are listed in table 2.3.

Compared to the lattice size parameter, there seems to be a disagreement in the reported values of the x- positional parameter of the O^1 oxygen at the 48f site.
Tabira et al. uses electron diffraction on a polycrystalline sample and claims that the difficulty in refining the value of x from X-ray diffraction data is a result of the low relative scattering power of the light oxygen atoms. Therefore Tabira et al. used CBED as means of x- parameter determination (Tabira et al. 2000). Lian et al. argues that the relative intensity of CBED could affect the accuracy of measured x values seeing that this method is sensitive to sample thickness variation, and that the variation in dynamic effects of electron diffraction is affected by various sample thicknesses (Lian et al. 2003)
The theoretical calculation undertaken by Minervini et al.(Minervini et al. 2002) and Taibra et al. (Tabira et al. 2000) underestimates the x- value compared to the experimental results. This deviation form experiment is explained by anti-site cation disorder (Tabira et al. 2000).

Year	Lattice parameter [Å]	x-parameter of the 48f site	Synthesis	Method	Reference
1964	10.069(1)	Not reported	Dry mix	XRD	(Brixner 1964)
1965	10.0762(6) 10.0759(10)	0.3300(10)	Dry mix	XRD	(Knop et al. 1965)
1969	10.0869(1)	0.3293(11)	Precipitation	XRD	(Knop et al. 1969)
2000	10.074(1)	0.331 0.325*	Dry mix	CBED *Calculated	(Tabira et al. 2000)
2002	Not reported	0.330(2)	Not reported	Calculated	(Minervini et al. 2002)
2003	10.0787(3)	0.3278(8)	Single crystal	XRD	(Lian et al. 2003)
2006	10.076(3)	0.3283(5)	Dry mix	XRD	(Lau et al. 2006)
2008	10.071(2) 10.072(2)†	Not reported	Wet (see section 2.2.2)	XRD	(Fjeld et al. 2008).

† Lattice size parameter of $Er_{1.96}Ca_{0.04}Ti_2O_{6.98}$

The effect on structure has been reported for over stoichiometry of erbium of x = 0.1-0.65 in $Er_{2+x}Ti_{2-x}O_{7-x/2}$. The lattice size parameter increases linearly from 10.116(6) Å to 10.2663(3) Å. The x- positional parameter increases linearly with the amount of excess erbium from to 0.3296(6) to 0.355(2). This means that the coordination of the oxygen to the anions approaches the tetrahedral coordination of the fluorite structure (Lau et al. 2006).

2.1.4 Defect chemistry

The dominating defects for $Er_2Ti_2O_7$ in the pyrochlore phase are predicted by energy minimization (Wilde and Catlow 1998; Minervini et al. 2000; Pirzada et al. 2001). It is reported that the cation anti-site defect has the lowest energy of the intrinsic defects. Here, the an A^{3+} cation is substituted on to a B site and a B^{4+} is substituted onto an A- site (Minervini et al. 2000). Refined data from x- ray diffraction indicate the existence of these defects (Lau et al. 2006; Shlyakhtina et al. 2007). The formation process can be described in Kröger- Vink notation for $Er_2Ti_2O_7$:

[2.1] $\quad Er_{Er}{}^{x} + Ti_{Ti}{}^{x} = Er_{Ti}{}' + Ti_{Er}{}^{\bullet}$
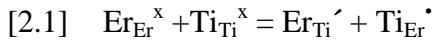
The other dominating intrinsic defect is the oxygen Frenkel pair. This consists of a vacancy on a 48f site and an interstitial on an 8a site. These defects have been identified by refinement of x-ray diffraction data (Lau et al. 2006; Shlyakhtina et al. 2007).

[2.2] $\quad O_O{}^{x} = v_{(48f)}{}^{\bullet\bullet} + O_{i(8a)}{}''$
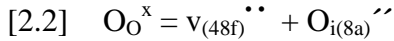
Cation disorder increases the similarity between nonequivalent oxygen sites. Reported calculations indicate that a cation anti-site pair adjacent to an oxygen Frenkel pair reduces the oxygen Frenkel formation energy greatly. The lowered energy of oxygen Frenkel pair formation around cation anti-site defects therefore produces defect clusters (Minervini et al. 2000):

[2.3] $\quad Er_{Er}{}^{x} + Ti_{Ti}{}^{x} + O_O{}^{x} = \{Er_{Ti}{}' + Ti_{Er}{}^{\bullet} + v_{(48f)}{}^{\bullet\bullet} + O_{i(8a)}{}''\}^{x}$

Acceptor doping of stoichiometric pyrochloric rare earth titanates by divalent calcium ions has been reported to increase the ionic conductivity by an increase of free mobile charge carriers (Kramer et al. 1994). $Er_{1.96}Ca_{0.04}Ti_2O_{6.98}$ exhibits predominantly oxygen ion conduction in grain interiors, while protons were found to play an important role as charge carriers in boundary related processes (Fjeld et al. 2008). The Ca^{2+} ions are expected to be situated at erbium positions. The proposed energetically favorable mechanism for incorporation of calsium ions is (Pirzada et al. 2003):

[2.4] $\quad 4CaO + 4Er_{Er}{}^{x} + 2O_O{}^{x} = 4Ca_{Er}{}' + 2v_O{}^{\bullet\bullet} + 2Er_2O_3$
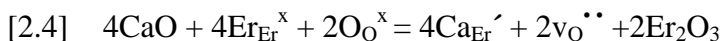
The oxygen ion migration pathways have been simulated for several oxide pyrochlores. Oxygen ion conduction proceeds via an oxygen vacancy mechanism for pyrochlores and fluorites (Tuller 1994). The most energetically favorable jumping mechanism for $Er_2Ti_2O_7$ has been predicted to be simple jumps between 48f sites in the <100> directions (Pirzada et al. 2001).

The presence of defects is therefore necessary for oxygen ion conduction and the conductivity increases if the defects density is increased. Probability of defect clustering increases with defect density. If the defect density is too large, it will reduce the ionic conductivity. There is believed to be an optimal defect density where the ionic conductivity reaches its maximum (Shlyakhtina et al. 2007).

2.2 Synthesis of $Er_2Ti_2O_7$ and $Er_{1.96}Ca_{0.04}Ti_2O_{6.98}$

2.2.1 Dry method

Er_2O_3 (REacton ® 99.99 % (REO)) powder was dried in a furnace at 800 ºC for 4h to remove unwanted H_2O. The dry powder was quickly put into an exicator. Stoichiometric amounts of TiO_2 (Alfa Aesar, 99.5 %) and $CaCO_3$ (Sigma-Aldrich, 99.95 %) were added. This mixture was milled by an agate ball-miller at 150rpm for 30 min, reversal every 5min, then dried and pressed to a tablet at a pressure of 314 MPa. The tablet was calcined over night and then ground in an agate mortar. The process was repeated trice at 850 ºC, 950 ºC and 1050 ºC. The resulting tablet was ground. Half the powder was then ball-milled and calcined at 1200 ºC over night.

Two tablets were pressed of the powder finally calcined at 1050 ºC and two of the powder finally calcined at 1200 ºC. One tablet of each final calcination temperature was sintered at 1500 ºC and one at 1580 ºC.

2.2.2 Wet method

Sample was prepared by H. Fjeld as reported elsewhere (Fjeld et al. 2008).
Er_2O_3 (REacton ® 99.99 % (REO)) or (Molycorp, 98 %, Ho main impurity) powder was dried in an oven for several hours to remove unwanted H_2O, and then dissolved in HNO_3 (6M) by constant heating and stirring. Then a stoichiometric amount of $CaCO_3$ was added together with citric acid a complexing agent. Subsequent decomposition of the citric acid produced a viscous solution. This solution was heated to 700 ºC which produced a pink powder. Then a stoichiometric amount of TiO_2 was added and the mixture was ball milled and calcined 800 ºC. Ball milling and calcination was repeated twice at 900 ºC – and 1000 ºC. Tablets were than pressed. The preparation of $Er_2Ti_2O_7$ followed the same route as described above except that no $CaCO_3$ was added.

2.2.3 Synthesis and density measurements

Density was calculated by the weight- volume ratio of the tablets, see table 2.4. Volume was estimated by mean diameter and height of the tablets. It is assumed that the shape of the tablets do not vary considerably from that of a perfect cylinder. Density seems to

increase with calcination and sintering temperature. Sample A, exhibited the highest density of all the samples. The color of sample A seems darker than the rest. All the other samples (sample B-D) were approximately of the same color, see figure 2.4.

Table 2.4: Measured mean density of the tablets. Each sample was assigned a letter A-D. Theoretical density is reported to be 7.04 g/ cm^3 (Knop et al. 1965).

Temperature of final calcination [ºC]	Sintering temperature [ºC]	Density [g/ cm^3]	Relative density [%]
A: 1200	1580	6.2	89
B: 1200	1500	5.6	80
C: 1050	1580	4.7	68
D: 1050	1500	4.2	60
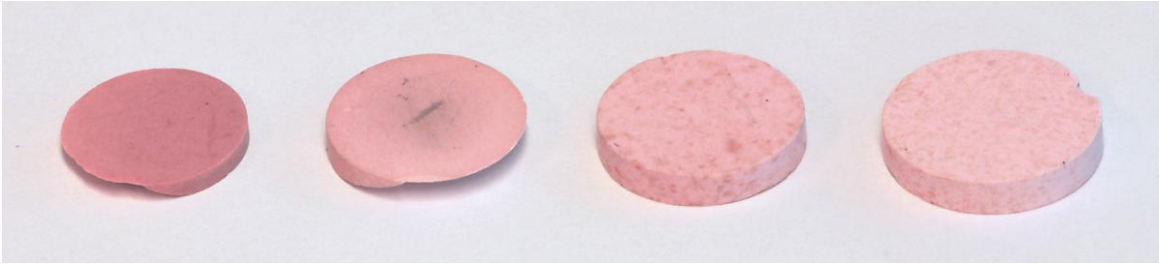
Figure 2.4: Sample A-D (left to right). Sample A (left) is darker than the other samples. This and the density measurements in table 2.4 indicate that this sample is the densest.

SEM was used to investigate the porosity of the surface of all four samples, see figure 2.5. This was done to confirm the reliability of the rather crude density measurement. The images indicate that the porosity of sample A (figure 2.5 A) was much less than sample B- D (figure 2.5 B-D). No significant difference was found in the porosity between the images of samples B- D. This indicates that they approximately obtained the same density. Ring shapes were observed in particles in all samples at higher magnifications, see figure 2.6.
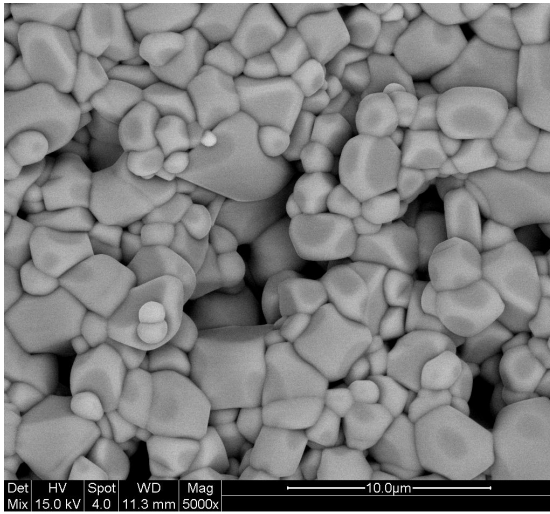
A)
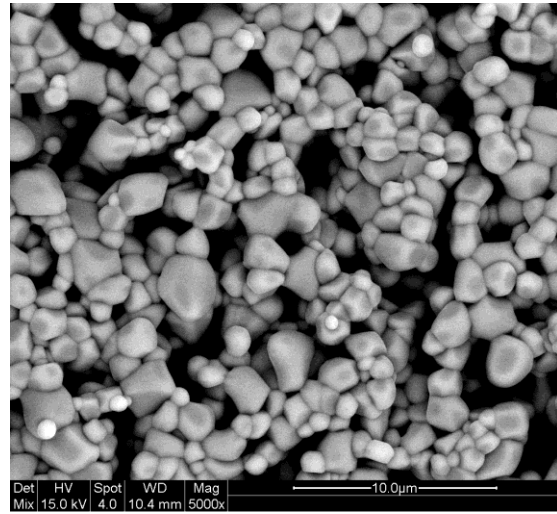
B)
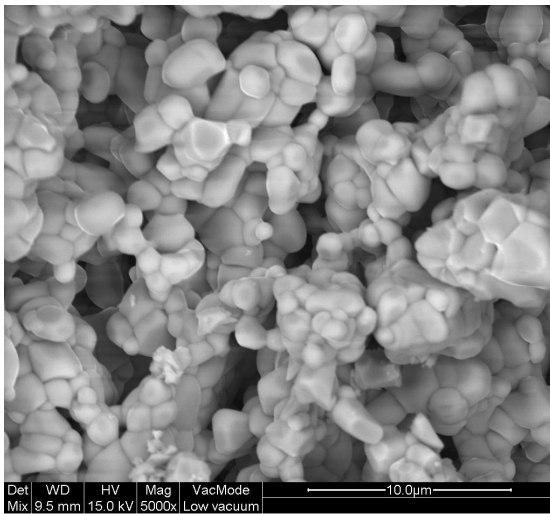
C)
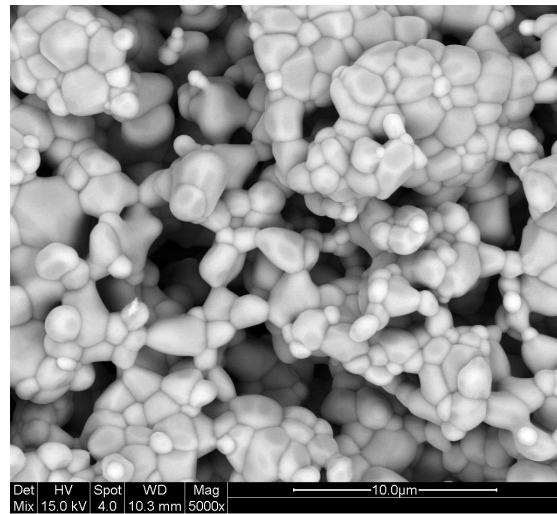
D)

Figure 2.5: SEM images of all four samples. The image of sample A appears less porous than the other samples. There is no significant difference between the images of sample B- D.
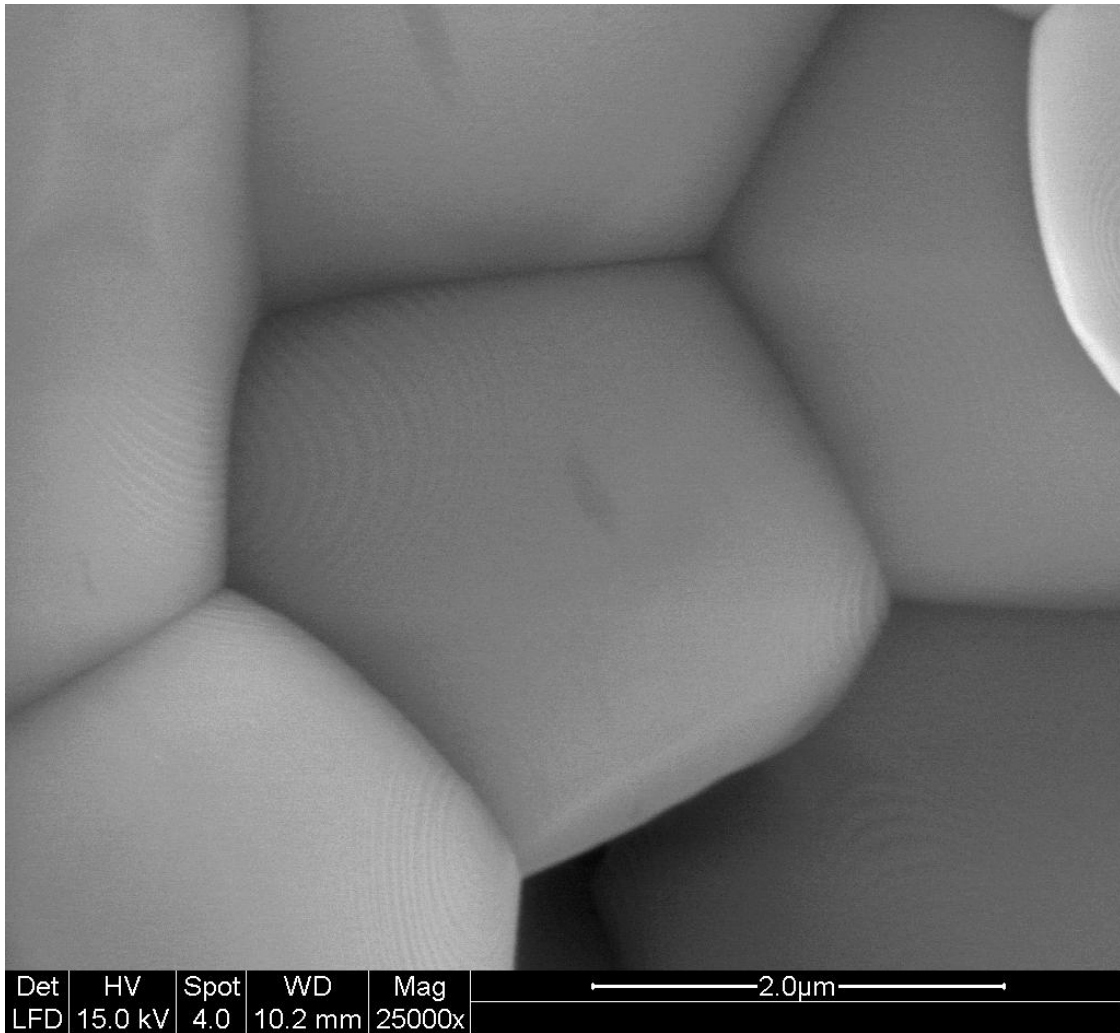
Figure 2.6: The ring shaped patterns observed in sample A-D.

2.3 Results

2.3.1 Determination of Bravais lattice

Both crushed and ion milled specimens were investigated to determine if heating during ion milling affected the structure significantly. The same TEM specimen as used in April 2007 was reexamined. Selected area diffraction patterns off these specimens were indexed in agreement with a face centered unit cell with size parameter a = 10.072(2) Å from XRD (Fjeld et al. 2008). Reflection conditions for the all SAD patterns, as seen in figure 2.7 and table 2.5, were found to be consistent with that of a face centered cubic Bravais lattice (Hahn 1983):

hkl: h + k, h + l, k + l = 2n
0kl: k, l = 2n
hhl: h + l = 2n
h00: h = 2n

These results are in disagreement with the student project of April 2007, see figure 2.1.
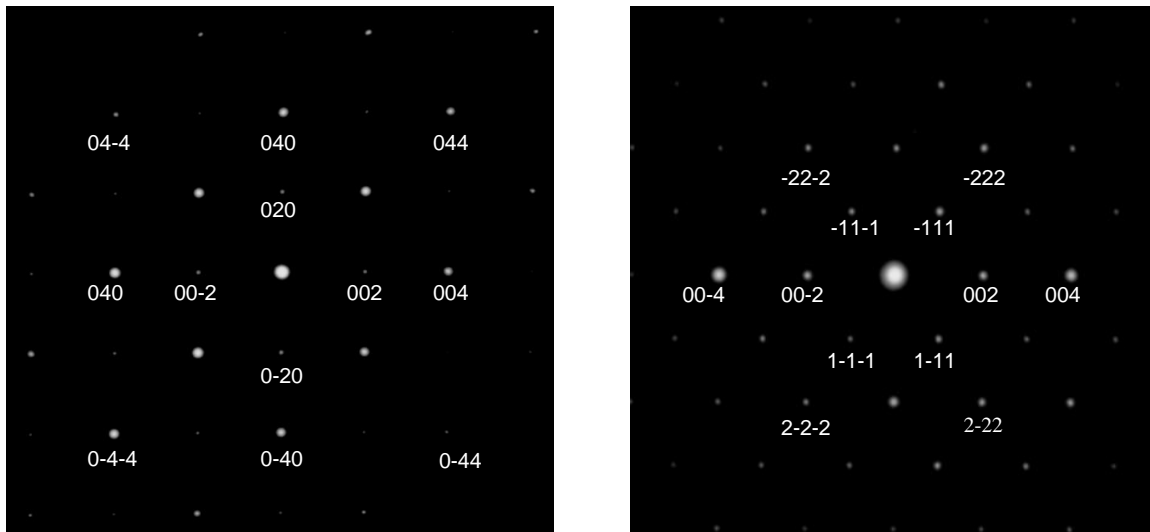
Figure 2.7: SAD patterns of the [100] projection (left) and the [110] projection (right). The strong reflections in the [100] projection are the 00l and 0kk reflections, where k, l = 4n. The strong reflections in the [110] projection are the 00l- type reflections where l = 4n.

Table 2.5: Measured SAD d- values compared to calculated d- values.

HKL	d- calculated [Å]	d- observed [Å]	RMS	Deviation [%]
111	5.8151	5.78	± 0.07	0.6
200	5.0360	5.01	± 0.09	0.5
220	3.5610	3.51	± 0.07	1.4
311	3.0368	3.00	± 0.05	1.2
222	2.9075	2.89	± 0.04	0.6
400	2.5180	2.50	± 0.04	0.7
331	2.3107	2.28	± 0.04	1.3

2.3.2 Determination of point group

The [100], [110] and [111] projections were chosen to determine the point group of $Er_{1.96}Ca_{0.04}Ti_2O_{6.98}$. In both CBED patterns of the [100] projection, four mirror planes separated by 45 degrees were observed, as seen in figure 2.8. This is referred to as 4mm WP- and BF projection symmetry respectively. Only three point groups exhibit this WP symmetry: 4mm, 4/mmm and m3m. In the CBED patterns of the [111] projection, see figure 2.9, three mirror planes separated by 60 degrees were observed in the pattern obtained at a small camera length. This is referred to as 3m WP symmetry. Six mirror planes separated by 30 degrees were observed in the pattern obtained at a large camera length. This is referred to as 6mm BF projection symmetry. Five point groups give rise to this WP symmetry: 3m, -3m, -43m, m3m and -62m. In both CBED patterns of the [110] projection, two mirror planes separated by 90 degrees were observed, see figure 2.10. This is referred to as 2mm WP- and BF projection symmetry respectively. This WP symmetry can be caused by one of these nine point groups: mm2, mmm, m3, m3m, 4/mmm, 6m2, 6/mmm, -42m and -43m. The only point group that is consistent with all observed WP symmetries (4mm, 3m and 2mm) is m3m. Observed WP- and BF

projection symmetries along with possible diffraction- and point groups are listed in table 2.6.

Table 2.6: Table of observed WP and BF symmetries and possible point groups for each zone axis. The only point group that is consistent with all observed WP symmetries is m3m.

Zone axis	WP symmetry	BF proj. symmerty	Possible diffraction groups	Possible point groups
[100]	4mm	4mm	4mm	4mm
			$4mm1_R$	4/mmm, **m3m**
[110]	2mm	2mm	2mm	mm2, -6m2
			$2mm1_R$	mmm, 4/mmm, 6/mmm, m3, **m3m**
			4_Rmm_R	-42m, -43m
[111]	3m	6mm	3m	3m, -43m
			$3m1_R$	-6m2
			6_Rmm_R	-3m, **m3m**
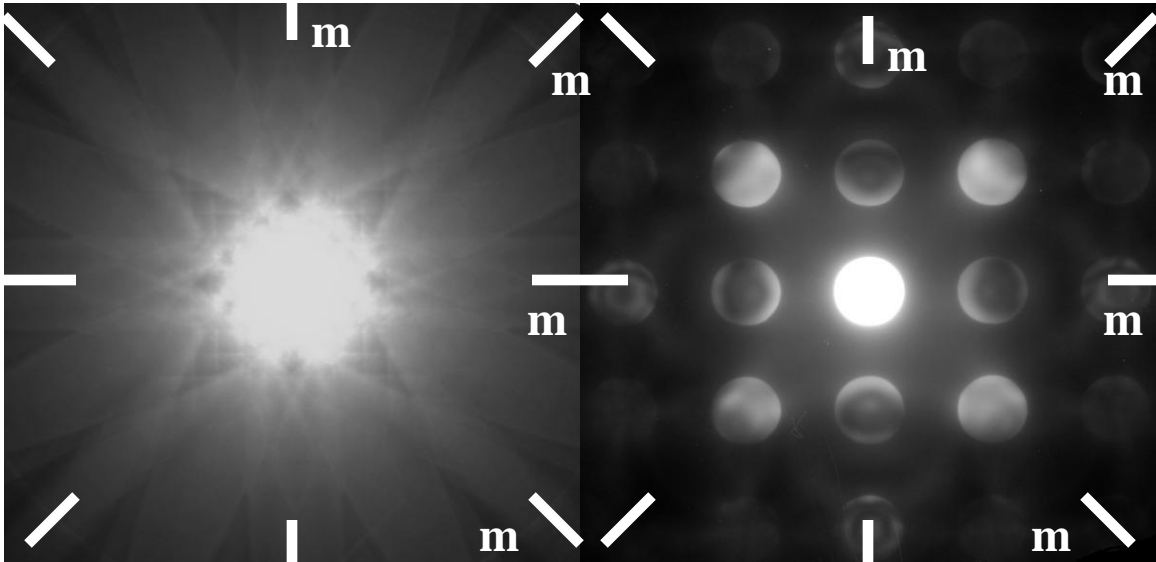
Figure 2.8: CBED patterns of the [100] projection. Four mirror planes separated by 45 degrees were observed in the pattern obtained at a small camera length (left). This is referred to as 4mm WP symmetry. Four mirror planes separated by 45 degrees were observed in the pattern obtained at a large camera length (right). This is referred to as 4mm BF projection symmetry.
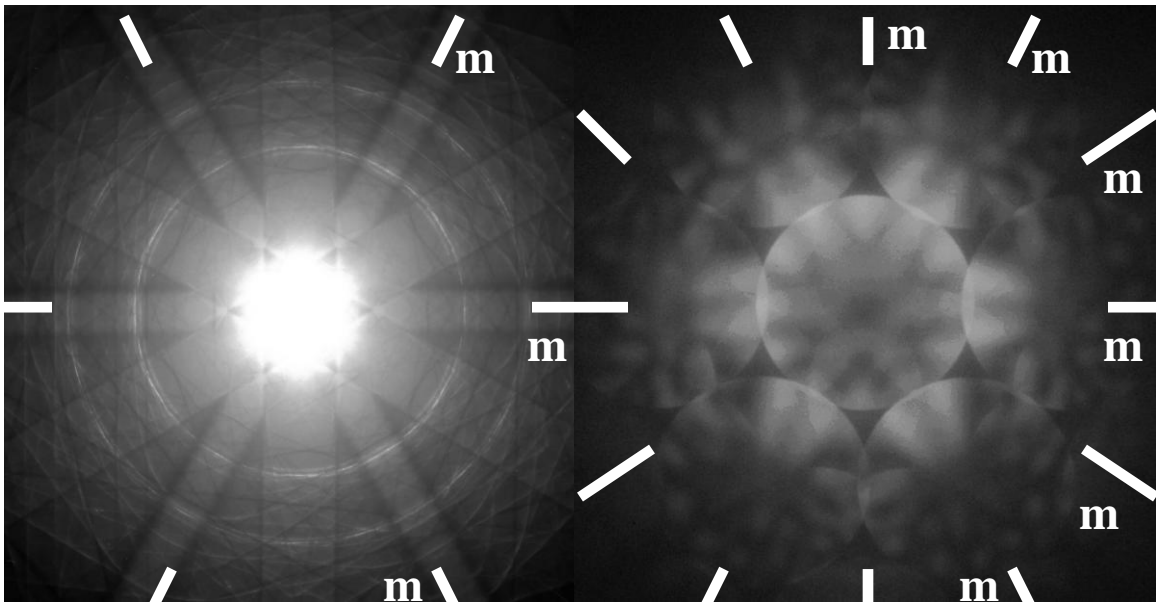
Figure 2.9: CBED patterns of the [111] projection. Three mirror planes separated by 60 degrees were observed in the pattern obtained at a small camera length (left). This is referred to as 3m WP symmetry. Six mirror planes separated by 30 degrees were observed in the pattern obtained at a large camera length (right). This is referred to as 6mm BF projection symmetry.
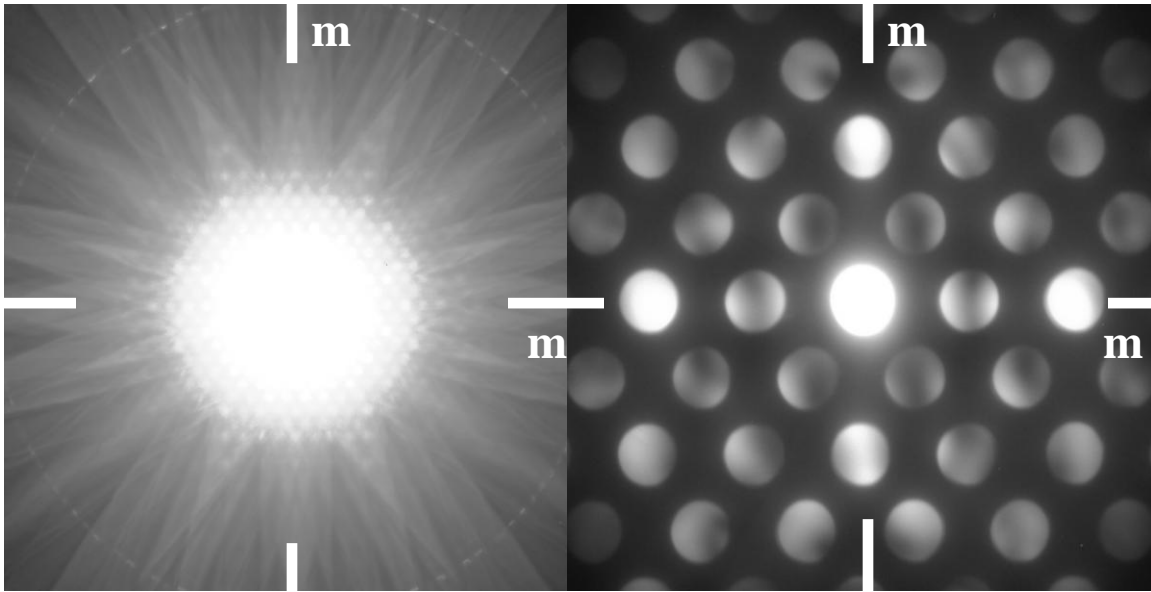
Figure 2.10: CBED patterns of the [110] projection. Two mirror planes separated by 90 degrees were observed in the pattern obtained at a small camera length (left). This is referred to as 2mm WP symmetry. Two mirror planes separated by 90 degrees were observed in the pattern obtained at a large camera length (right). This is referred to as 2mm BF projection symmetry.

2.3.3 Determination of space group

The space group of the crystal structure is consistent with a face centered cubic Bravais lattice, see section 2.3.1, and the m3m point group, see section 2.3.2. Only four space groups satisfy these criteria: Fm3m (no. 225), Fm3c (no. 226), Fd3m (no. 227) and Fd3c (no. 288) (Hahn 1983). These space groups are distinguishable by their translational symmetry operations.

The reflections conditions for the SAD patterns, as seen in figure 2.7, revealed no indication of glide plains or screw axis in addition to that of a face centered Bravais lattice (Hahn 1983). The Kossel Möllenstedt pattern of the [110] projection included GM B_2 lines in the 002 and 00-2 reflection discs, as seen in figure 2.11, which is caused by a 4_1 or a 4_3 screw axis (Hahn 1983). This reduces the possible space groups to two: Fd3m (no. 227) and Fd3c (no. 288), which both exhibits the 4_1 screw axis.

It is expected that titanium- and erbium/ calcium- ions mainly occupy different Wyckoff positions due to the difference in size and in oxidation state (Minervini et al. 2000; Pirzada et al. 2003) The unit cell contains eight formula units (Subramanian 1993) of $Er_{1.96}Ca_{0.04}Ti_2O_{6.98}$, so the multiplicity of each cation site should be 16. Fd3m contains two Wyckoff positions of multiplicity 16, while Fd3c contains only one. Therefore the only space group that can accommodate for the limits set by stoichiometry and also fit with all experimental observations is Fd3m, which is the reported space group for $Er_2Ti_2O_7$ (Knop et al. 1965; Knop et al. 1969; Subramanian et al. 1983).
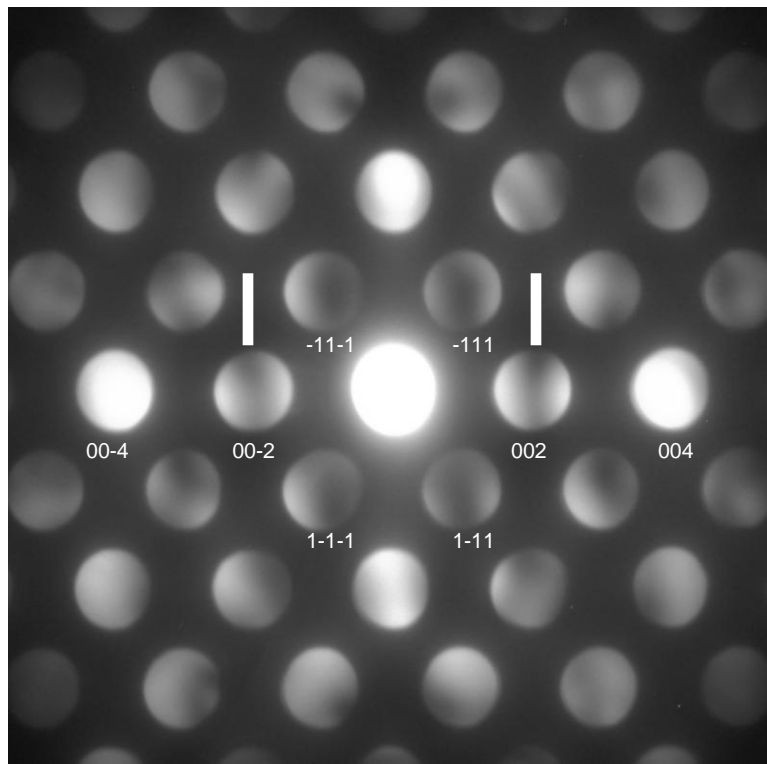
Figure 2.11: CBED pattern of the [110] projection. GM B_2 lines in the 002 and 00-2 reflection discs are indicated by lines.

2.3.4 Investigation of the apparent change in Bravais lattice

The previous investigations did not repeat the SAD patterns for a primitive Bravais lattice observed in April of 2007, see figure 2.1. This inconsistency may be caused by many factors:

- Impurities in reagents
- Calcium doping
- Phase transition
- Ordering of defects
- Water content
- The synthesis

The effect of these factors ob the Bravais lattice was investigated in the subsequent sections.

2.3.4.1 Ca doping and impure Er_2O_3

The Ca ions are smaller than the Er ions and are expected to be situated at the erbium positions (Pirzada et al. 2003). The result of this may be a distortion of the structure relative to the un-doped compound.

The original sample was made with 98 % Er_2O_3 (Molycorp, main impurity Ho) and prepared by the wet method, see section 2.2.2. Specimens were prepared by ion milling. Erbium- and holmium- ions are close in size. Ho ions are therefore expected to be situated at the Er positions. This might effects the overall symmetry of the crystal structure. To determine the contribution of Er_2O_3 purity and Ca^{2+} doping to the crystal structure, three samples were investigated:

- $Er_{1.96}Ca_{0.04}Ti_2O_{6.98}$, made with 99.99 % Er_2O_3
- $Er_2Ti_2O_7$, made with 99.99 % Er_2O_3
- $Er_2Ti_2O_7$, made with 98 % Er_2O_3

XRD data from all three samples exhibited a single phase consistent with what is reported for $Er_2Ti_2O_7$ (Subramanian et al. 1983), as seen in figure 2.13. SAD patterns off all three

samples obtained at eucentric height indicate a face centered cubic Bravais lattice as seen in figure 2.12. Plane distances measured in both XRD and SAD agreed with the reported values for $Er_2Ti_2O_7$. These results indicate that neither Ca doping nor Ho impurities give rise to any observable change in the Bravais lattice of the crystal relative to the specimen which exhibited a primitive lattice in 2007

A)

B)

C)

D)
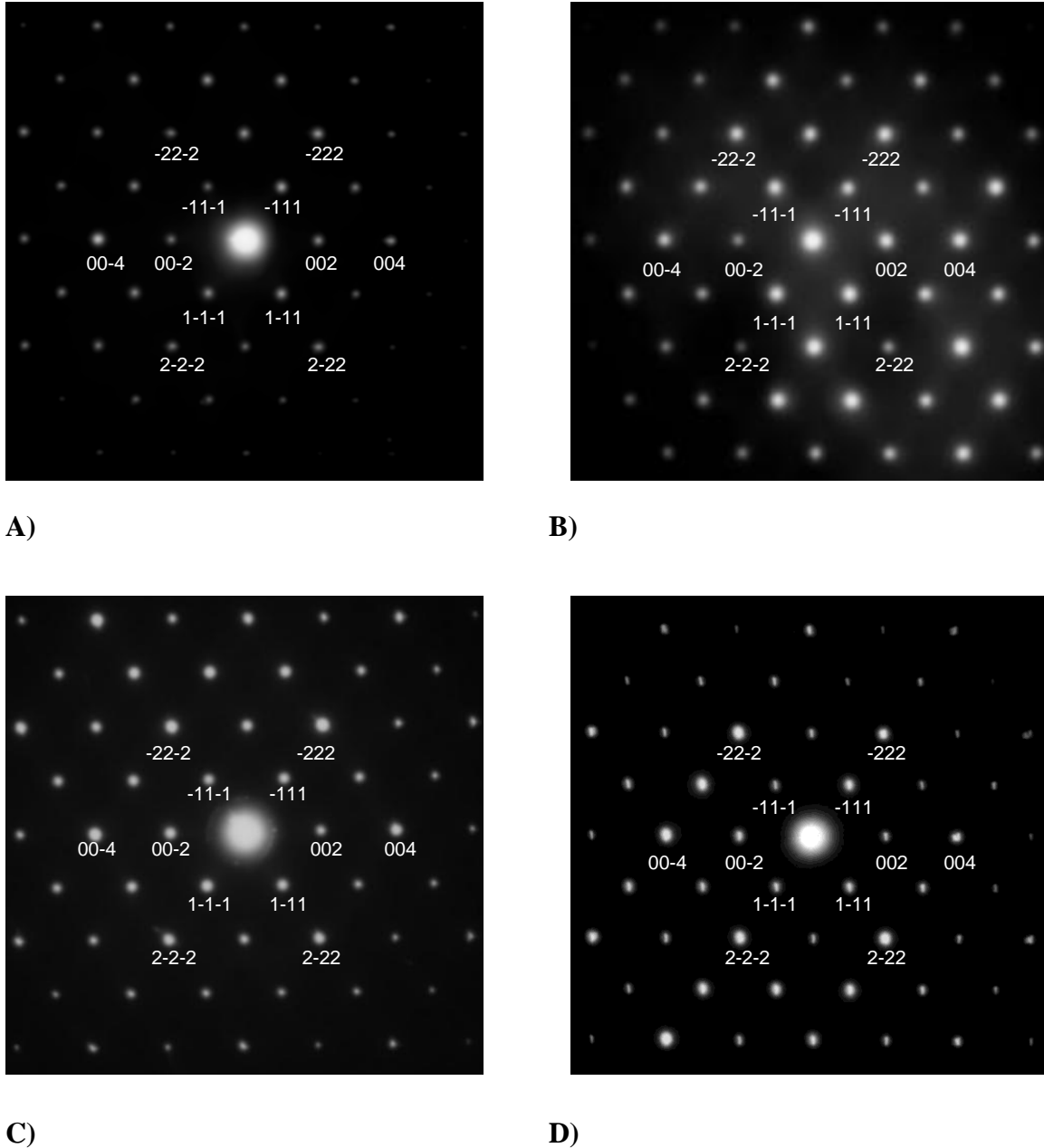
Figure 2.12: SAD patterns the [110] projection. A) (original sample) $Er_{1.96}Ca_{0.04}Ti_2O_{6.98}$ made by 98 % Er_2O_3 B) $Er_{1.96}Ca_{0.04}Ti_2O_{6.98}$, made by 99.99 % Er_2O_3 C) $Er_2Ti_2O_7$, made with 99.99 % Er_2O_3 D) $Er_2Ti_2O_7$, made with 98 % Er_2O_3. All reflections are consistent with the selection rules for a face centered cubic Bravais lattice.
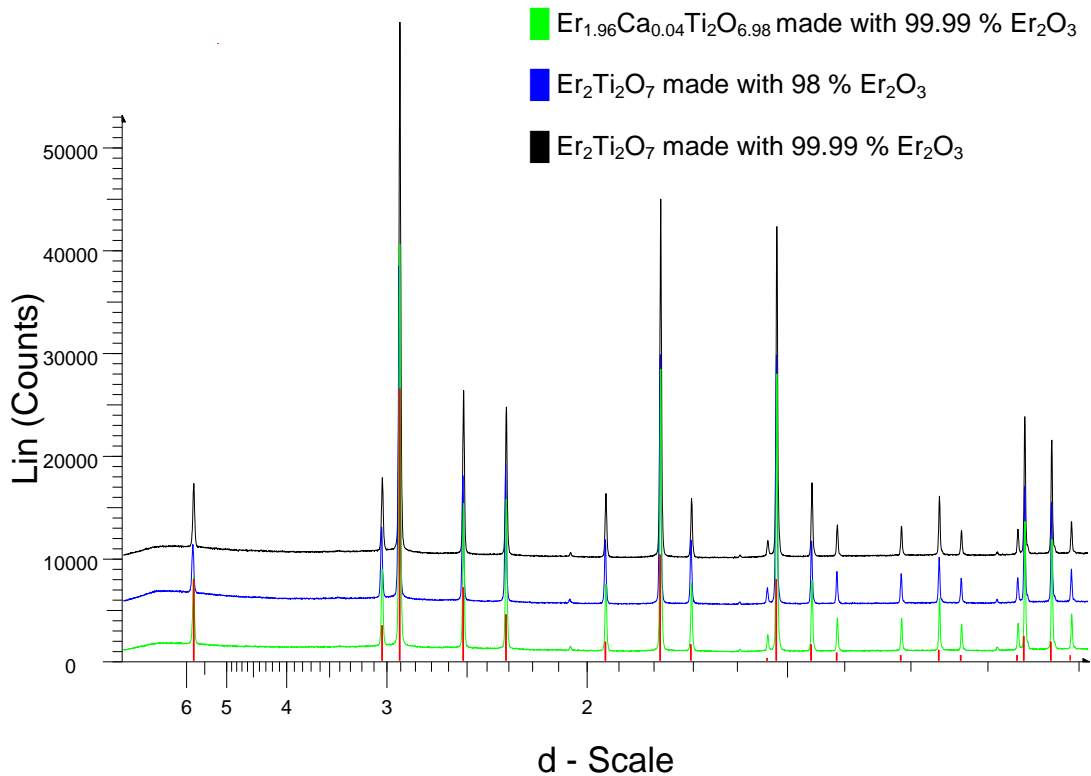
Figure 2.13: XRD diffractogram of the samples made with different Er_2O_3 powder. The red bars indicate the lattice plane distance [Å] reported for $Er_2Ti_2O_7$ (Knop et al. 1965).

2.3.4.2 Phase transition, order- disorder transition and water absorption

A slow transition from a primitive high- temperature phase to a face centered room- temperature phase might explain the apparent change in Bravais lattice. This phase transition should be reversible by heat treatment.

Defects are formed during calcination and sintering. Disordered defects might lower the symmetry of the structure. This decrease in symmetry may cause the observed primitive Bravais lattice. Over time, the transition to a face centered Bravais lattice might be explained by the ordering of defects, which would increase overall symmetry. This transition might be reversible by heat treatment.

Er_2O_3 is hygroscopic (Aeasar 2008) and it is therefore possible that $Er_{1.96}Ca_{0.04}Ti_2O_{6.98}$ absorbs water. This absorption might affect the crystal structure as water might be absorbed by the structure over time. Water is most likely removable by heat treatment.

These hypotheses were investigated by heat treatment and subsequent SAD analysis. The sample which exhibited a primitive lattice in 2007 was heated to 1126 ℃ for 5 hours and then to 1500 ℃ for 5 hours. 1500 ℃ is the sintering temperature. The sample was investigated by SAD after each heat treatment. Specimens were prepared by the crushing technique. After the heat treatment, the resulting SAD patterns indicated a face centered Bravais lattice as seen in figure 2.14.
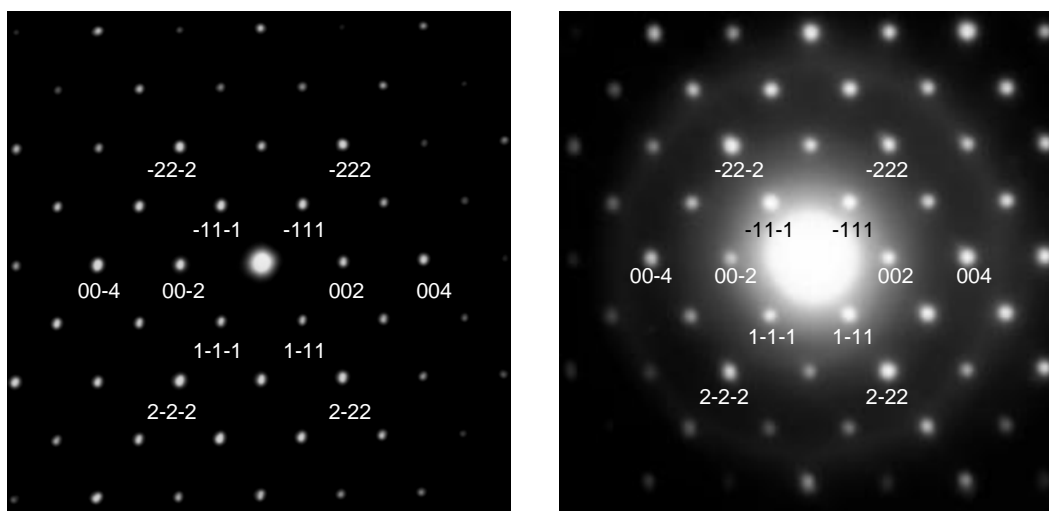
Figure 2.14: SAD patterns the [110] projection. The sample heated to 1126 ℃ (left) and then to 1500 ℃ (right). All reflections are consistent with the selection rules for a face centered Bravais lattice.

2.3.4.3 Dry method of synthesis

Different methods of synthesis might affect the resulting composition and thereby the Bravais lattice of the structure. It was therefore of interest to obtain SAD patterns and XRD diffractograms of samples prepared by the dry method of synthesis.

Samples were prepared by the "dry" method described on in section 2.2.1. The powdered sample with a final calcination temperature of 1050 ℃ was investigated by XRD. The diffractogram (figure 2.15) indicated that three distinct phases were present in

46

the sample: Er_2O_3, TiO_2 (rutile) and the $Er_2Ti_2O_7$ pyrochlore phase. The reported d-values and peak intensities of $Er_2Ti_2O_7$ was in agreement with the present data for the $Er_{1.96}Ca_{0.04}Ti_2O_{6.98}$ phase, and was therefore used for phase identification.

The crushed sample with a final calcination temperature of 1200 ºC was investigated by XRD. This diffractogram (figure 2.16) indicated that only the pyrochlore phase was present. Some of the low intensity peaks might be interpreted as originating from a small amount of Er_2O_3 in the sample. There were no detectable peaks originating from any allotropes of TiO_2. Intensity measurements of the peaks observed in this diffractogram fits reasonably with calculated peak intensities of $Er_2Ti_2O_7$ from the PDFMaintEx library which are based on Knop et al. (Knop et al. 1965) and intensities calculated by the ATOMS 5.1 software , see table 2.7. This indicates that $Er_2Ti_2O_7$ and $Er_{1.96}Ca_{0.04}Ti_2O_{6.98}$ obtain the same phase.
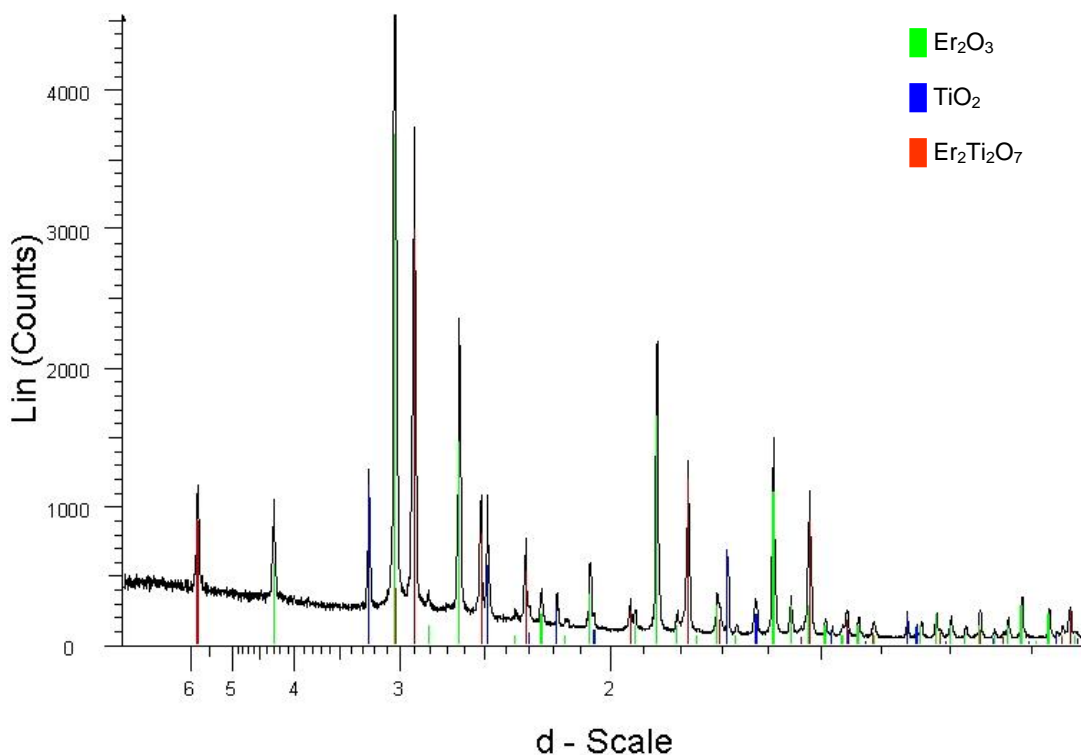
Figure 2.15: XRD diffractogram of the $Er_{1.96}Ca_{0.04}Ti_2O_{6.98}$ powder with a final calcination temperature of 1050 ºC. Peaks which originate from Er_2O_3, TiO_2 (synthetic rutile) and $Er_2Ti_2O_7$ are indicated by color.
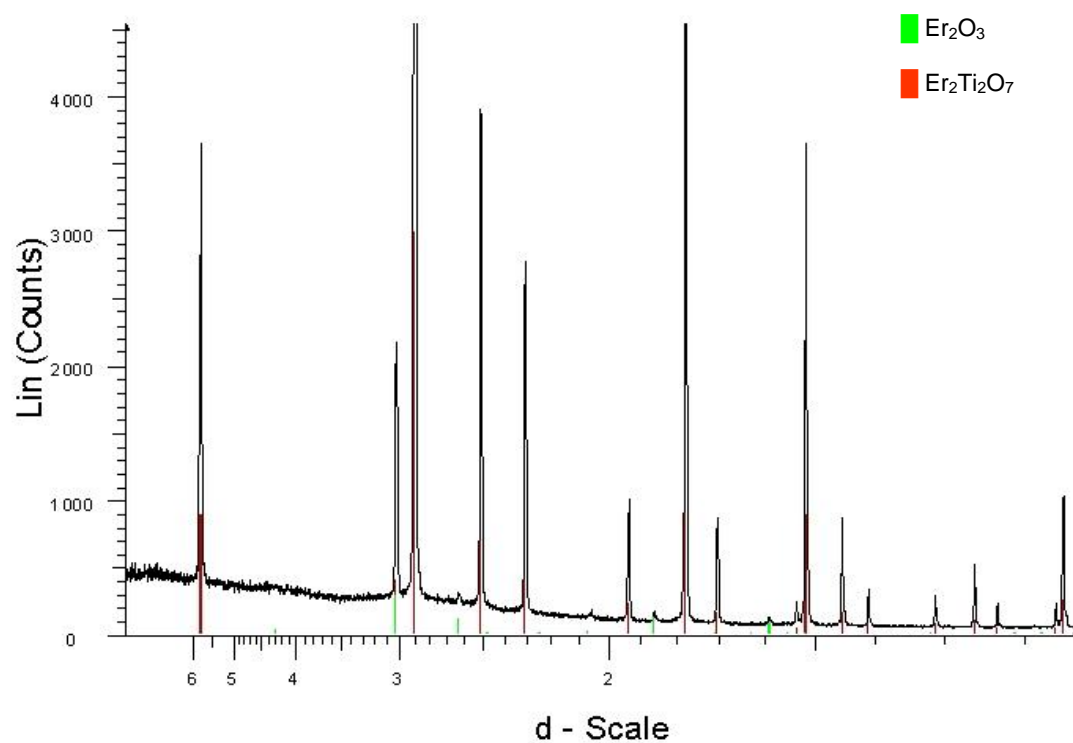
Figure 2.16: XRD diffractogram of the $Er_{1.96}Ca_{0.04}Ti_2O_{6.98}$ powder with a final calcination temperature of 1200 ºC. Peaks which originate from Er_2O_3 and $Er_2Ti_2O_7$ are indicated by color.

Table 2.7: Calculated plane distances and intensities. The observed intensities of the sample with a final calcination temperature of 1200 °C fit reasonably with the calculated intensities and calculated intensities from literature (Knop et al. 1965). This indicates that $Er_2Ti_2O_7$ and $Er_{1.96}Ca_{0.04}Ti_2O_{6.98}$ obtain the same phase.

HKL	d-calculated [Å]	I- observed	I- calculated	I- calculated*
111	5.8151	23	35	30
220	3.5610	0	0	0
311	3.0368	14	19	14
222	2.9075	100	100	100
400	2.5180	25	29	27
331	2.3107	18	21	18
422	2.0559	1	0	0
511	1.9384	6	9	8
440	1.7805	37	39	40
531	1.7025	6	8	6
620	1.5925	1	0	0
533	1.5360	1	2	2
622	1.5184	26	30	30
444	1.4538	6	7	6
711	1.4104	2	2	3
642	1.3459	2	0	3
731	1.3113	4	2	4
800	1.2590	1	4	2
733	1.2305	0	2	0
822	1.1870	1	0	2
751	1.1630	8	2	9

* Intensities calculated from literature (Knop et al. 1965)

Four samples were pressed into tablets and sintered. They are herby referred to as:

- sample A: calcined at 1200 °C and sintered at 1580 °C
- sample B: calcined at1200 °C and sintered at 1500 °C
- sample C: calcined at 1050 °C and sintered at 1580 °C
- sample D: calcined at 1050 °C and sintered at 1500 °C

The sample A and sample D were both investigated by TEM. Both specimens were prepared by the crushing method. SAD patterns from both specimens were obtained at eucentric height and indicated a face centered cubic Bravais lattice as seen in figure 2.17.
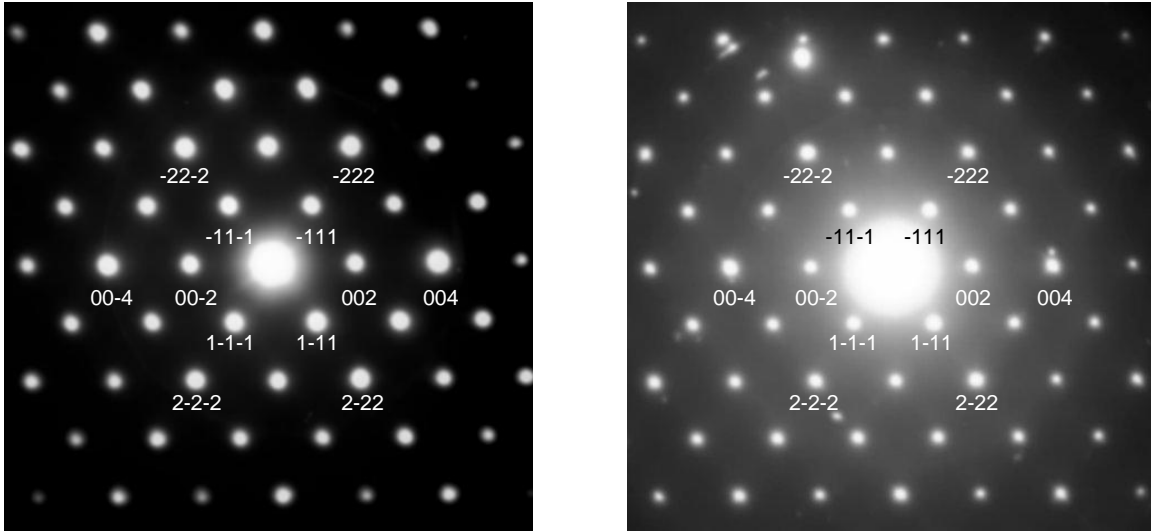
Figure 2.17: SAD patterns of the [110] projection of sample A (left) and sample D (right). Both patterns satisfy the reflection conditions of a face centered Bravais lattice.

2.4 Discussion

2.4.1 Synthesis and density measurements

Different temperatures of calcination and sintering during the dry method of synthesis might affect the composition and density of the samples. This was investigated by XRD, SEM and density measurements. XRD data indicate that samples prepared by the dry method and calcined with a final temperature of 1050 ℃ contained the pyrochlore phase as well as Er_2O_3 and rutile. The samples calcined at a final temperature of 1200 ℃ contained the pyrochlore phase as well as traces of Er_2O_3. The measured density of the samples (A- D) prepared by the dry method was found dependent on calcination and sintering temperature. The higher the temperatures the denser the sample, see table 2.4. The SEM images of the surface of sample A indicated a lower porosity than samples B-D. The difference in porosity observed by SEM of samples B- D did not appear to be significant. It should be noted that SEM investigates the surface and might be misleading as to the bulk density of the samples. These results suggest that an approximate single phase should be obtained by calcination to produce a sample with a relative density of ~ 90 % by sintering.

The ring shaped structures observed in the particles off samples A- D by SEM might be caused by the crystal growth during calcination or mechanical deformation. Mechanical deformation might be caused by sintering. An explanation might also be a combination of the above mentioned factors. No investigation has been undertaken to determine the cause of this phenomenon.

2.4.2 Bravais lattice

The selected area diffraction patterns obtained in April 2007 have not been repeated. They indicated a primitive Bravais lattice. All SAD patterns obtained since April 2007, indicate that $Er_{1.96}Ca_{0.04}Ti_2O_{6.98}$ and $Er_2Ti_2O_7$ exhibit a face centered cubic Bravais lattice. SAD and CBED patterns indicated that $Er_{1.96}Ca_{0.04}Ti_2O_{6.98}$ crystallize in the Fd3m (no. 227) space group. This is consistent with the reported pyrochlore structure of $Er_2Ti_2O_7$ (Knop et al. 1965; Knop et al. 1969; Subramanian et al. 1983). No explanation of the primitive Bravais lattice indicated in April 2007 has been found. All investigated samples are listed with relevant parameters in table 2.8. The apparent change in Bravais lattice might be caused by one or more of the following factors:

- Impurities in reagents
- Calcium doping
- Phase transition
- Ordering of defects
- Water content
- The synthesis

The structural implications of these factors will be discussed in the following sections.

Table 2.8: All investigated samples of $Er_{1.96}Ca_{0.04}Ti_2O_{6.98}$ and $Er_2Ti_2O_7$. All parameters of the samples are listed for comparison. Heat treatment refers to thermal treatment after sintering.

Sample	Ca^{2+}	Er_2O_3 purity in %	Synthesis	Final calcination temp. [ºC]	Sintered [ºC]	Heat treatment [ºC]	Bravais Lattice	Phases detected by XRD
1.1	Y	98	Wet	1000	1500	X	*P/F	X
1.2	Y	98	Wet	1000	1500	1126	F	X
1.3	Y	98	Wet	1000	1500	1500	F	X
2	Y	99.99	Wet	1000	1500	X	F	Pyrochlore
3	N	98	Wet	1000	1500	X	F	Pyrochlore
4	N	99.99	Wet	1000	1500	X	F	Pyrochlore
A	Y	99.99	Dry	1200	1580	X	F	Pyrochlore + Er_2O_3 traces †
B	Y	99.99	Dry	1200	1500	X	F	Pyrochlore + Er_2O_3 traces †
C	Y	99.99	Dry	1050	1580	X	F	Pyrochlore + Er_2O_3 + rutile †
D	Y	99.99	Dry	1050	1500	X	F	Pyrochlore + Er_2O_3 + rutile †

* The primitive (P) Bravais lattice was observed during the student project in 2007 (Viegen, 2007 #31). The same sample was reinvestigated and found to exhibit a face centered cubic Bravais lattice. †Phases identified by XRD for sample A- D were identified after final calcination and not after sintering.

2.4.3 Calcium doping and holmium impurities

The incorporation of Ho impurities in the structure might affect the Bravais lattice. Samples were examined to determine the possible contribution of Ho impurities to the structure of $Er_2Ti_2O_7$ and $Er_{1.96}Ca_{0.04}Ti_2O_{6.98}$. These samples were prepared by the "wet method" with different Er_2O_3 powders as described in 3.2.

SAD patterns of all four samples indicated a face centered Bravais lattice. XRD data revealed no additional peaks, significant changes in peak intensity or additional phases for any of the samples. These results indicate that the holmium impurities in the Er_2O_3 powder do not affect the lattice Bravais lattice of $Er_2Ti_2O_7$. This might be explained as follows: Ho (no. 67) is placed next to Er (no. 68) in the periodic table of elements. Holmium ions are, as erbium ions, trivalent. Thus it is more likely that Ho mainly occupy Er sites rather than Ti sites in the structure. This is not likely to cause any significant breakdown of symmetry and thereby affect the Bravais lattice.

Acceptor doping of $Er_2Ti_2O_7$ by divalent calcium ions might distort the structure and thereby affect the Bravais lattice. SAD patterns of $Er_2Ti_2O_7$ and $Er_{1.96}Ca_{0.04}Ti_2O_{6.98}$ were obtained. Samples were prepared by the "wet method" and 99.99 % Er_2O_3. SAD patterns of the samples indicated a face centered Bravais lattice. No significant changes in intensity of the peaks, no additional peaks or phases were found by XRD. Reported refinement of XRD data concludes with no significant change of the lattice size parameter induced by calcium doping of $Er_2Ti_2O_7$, a = 10.0762(2) Å, to $Er_{1.96}Ca_{0.04}Ti_2O_{6.98}$, a = 10.072(2) Å (Fjeld et al. 2008). The structural effect of calcium doping might be explained as follows: Calcium ions are expected to occupy Er sites (Pirzada et al. 2003). The difference in valence of erbium and calcium is expected to induce oxygen vacancies and thereby might distort the structure. No evidence has been found which supports that calcium doping induces a significant breakdown of symmetry which affects the Bravais lattice.

The combination of acceptor doping and impurities in Er_2O_3 give rise to distortion of the structure and thereby might affect the Bravais lattice. SAD patterns of $Er_{1.96}Ca_{0.04}Ti_2O_{6.98}$ were obtained. The sample was prepared by the "wet method" and 98 % Er_2O_3. The patterns indicated a face centered Bravais lattice. This result indicates that a combination of acceptor doping and holmium impurities does not cause a significant distortion of the structure of $Er_2Ti_2O_7$ which affects the Bravais lattice.

2.4.4 Phase transition, order- disorder transition of defects and water content

A slow temperature dependent transition from a primitive high temperature phase to a face centered room temperature phase should be reversible by heat treatment. If the conditions during sintering are repeated, this should result in a transition to the high temperature phase.

Defects are formed during synthesis. The main defects formed are oxygen vacancies and cation anti- site defects, see 2.1.4. If there is a random distribution of defects in the lattice, this might reduce the overall crystallographic symmetry. The transformation from a primitive lattice to a face centered lattice might be explained by a disorder- to- order transition. Such an ordered state must be thermodynamically favorable at room temperature.

If the sample is quenched to room temperature and there exists a kinetic barrier slowing the transition rate sufficiently, it might be possible to detect the high temperature phase. If the selected area diffraction patterns of the heat treated sample indicated a primitive lattice, there is reason to believe that one or both of these transitions takes place.

If water was absorbed over time, this might affect the structure. Water is probably removable by heat treatment. By removing the water, structural effects caused by the water mighty be reversed. This might be observed by SAD if the rate of water absorption from the air is too slow for it to affect the analysis.

These hypotheses were tested by heat treatment. The sample which originally exhibited indications of a primitive lattice was heated to 1126 ºC and then to 1500 ºC. 1500 ºC is the sintering temperature. The resulting SAD patterns indicating a face centered Bravais lattice. Thus no SAD patterns confirmed the existence of a phase transition at 1126 ºC or 1500 ºC. This result is in agreement with the literature on the pyrochlore structure of $Er_2Ti_2O_7$ (Brixner 1964; Knop et al. 1965; Knop et al. 1969; Subramanian et al. 1983)). No primitive phase has been reported for this composition in the $Er_2O_3 - TiO_2$ system (Shcherbakova et al. 1979). If disordered defects affected the Bravais lattice of the structure, this would be observed in the SAD patterns. Thus no evidence has been found to support the hypothesis of a slow disorder- to- order transition of defects affecting the Bravais lattice of the structure. One or both of these transitions might still occur, but the

transition rate to a room temperature phase or an ordered defect configuration would then be too fast to make time for obtaining SAD patterns. This would be in disagreement with the SAD patterns obtained in April 2007, see figure 2.1. The heat treatment is likely to remove absorbed water. Therefore no evidence was found that suggests that water absorption affects the Bravais lattice of the structure.

2.4.5 Synthesis

Different methods of synthesis might also affect the resulting composition and thereby the overall symmetry of the samples. This was investigated by XRD and SAD. XRD patterns were obtained from the samples prepared by the dry-method and the wet-method. Diffractograms of samples prepared by the wet method only indicated the pyrochlore phase. XRD data indicated the sample prepared by the dry method and calcined at a final temperature of 1050 ºC contained the pyrochlore phase as well as Er_2O_3 and rutile. The samples prepared by the dry method and calcined at a final temperature of 1200 ºC contained the pyrochlore phase as well as traces of Er_2O_3. A sintering temperature of 1500 ºC or 1580 ºC will therefore probably result in a single phase sample if prepared by the dry method. Samples of $Er_{1.96}Ca_{0.04}Ti_2O_{6.98}$ which were prepared by both the wet- and dry method of synthesis were investigated by TEM. SAD patterns from all examined samples indicated a face centered cubic Bravais lattice. Thus no evidence supports the hypothesis that different methods of synthesis affect the observed Bravais lattice of $Er_{1.96}Ca_{0.04}Ti_2O_{6.98}$.

2.5 Conclusions

- A single phase material obtained by calcination is necessary to produce a sample of ~90 % relative density by sintering.

- $Er_{1.96}Ca_{0.04}Ti_2O_{6.98}$ was determined by SAD and CBED to crystallize in the Fd3m space group. This is in agreement with the structure reported for $Er_2Ti_2O_7$ (Knop et al. 1965; Knop et al. 1969; Subramanian et al. 1983).

- The SAD patterns which indicated a primitive Bravais lattice have not been repeated during this investigation.

- SAD patterns indicated that neither acceptor doping by divalent calcium ions nor holmium impurities or a combination of this affect the Bravais lattice of the structure.

- No phase transitions which affect the Bravais lattice have been indicated by SAD patterns subsequent to heat treatment at 1126 ℃ or at 1500 ℃.

- No order- disorder transition which affect the Bravais lattice have been indicated by SAD patterns subsequent to heat treatment at 1126 ℃ or at 1500 ℃.

- No change in the Bravais lattice has been indicated by SAD subsequent to heat treatment at 1126 ℃ or at 1500 ℃. Thus no evidence suggests that water absorption affected the Bravais lattice.

- SAD patterns indicated that neither method of synthesis affected the Bravais lattice of the structure of $Er_{1.96}Ca_{0.04}Ti_2O_{6.98}$.

2.5.1 Suggestions for further work

- Investigate the distortion of the structure as a function of calcium content. Proposed methods are IR- spectroscopy, TEM and XRD.

- Investigate cross section samples prepared by the dry method to determine if the surface porosity is typical for the bulk. Proposed method is SEM.

- Prepare samples by the wet method described in 2.2.2 to reproduce the SAD pattern indicating a primitive Bravais lattice.

Chapter 3

Lanthanum tungstate

3.1 Introduction and literature

No description of the structure of stoichiometric La_6WO_{12} has been found in literature. La_6WO_{12} has been reported to exhibit a relatively high proton conductivity of $3\text{-}5*10^{-3}$ S/cm in a wet atmosphere under 900 ℃. It is assumed that oxygen ions in the oxygen sublattice, O_O^x, yield an intrinsic anti- Frenkel disorder when they exchange with vacant interstitial positions, v_i^x, around the W centered octahedron:

[3.1] $O_O^x + v_i^x = v_O^{\bullet\bullet} + O_i''$
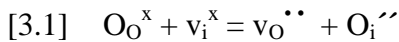
Then the proton conductivity then might be explained by:

[3.2] $H_2O\ (g) + v_O'' + O_O^x = 2OH_O^{\bullet}$

At high temperatures this compound exhibits n- type conductivity under reducing conditions and p-type conduction under oxidizing conditions (Haugsrud 2007; Haugsrud and Kjølseth 2008).

A series of samples of the $La_2O_3 - WO_3$ system have been investigated with nominal La/W ratio from 4.8 to 6.0. The samples were prepared by freeze drying synthesis, see 3.2. The compounds with a nominal La/W ratio of 4.8- 5.2 was found to segregate a $La_2W_2O_{12}$ phase and the compounds with a nominal La/W ratio of 5.8 and 6 were found to segregate a La_2O_3 phase. The compounds with a nominal La/W ratio of 5.0- 5.7 were found to obtain a single phase. The space group of $2.8 \bullet La_2O_3$ -WO_3 was proposed to be F-43m (no. 216) by XRD and NPD. Magrasó et al. experienced difficulties in refining all tungsten positions. In an attempt to solve this, low intensity peaks in the real space electron density of the 4d- and 24f Wyckoff positions were accredited to 0.66 tungsten ions per unit cell. The size of the unit cell is accredited to make the detection of these "missing" tungsten ions near or beyond the limit of x-ray- and neutron powder diffraction. Refined positions and occupancy can be seen in table 3.1. Composition is

reported to be $La_{26.5}W_{4.7(4)}O_{52.8(9)}$ with a lattice size parameter of a = 11.1868(3) Å. All phase identification and space group determination was done by XRD and NPD (Magrasó et al. 2009). This structure resembles the structure reported for $Y_6ReO_{14-\delta}$ (Ehrenberg et al. 2004) and differs significantly from the reported structure of Y_6WO_{12} and Ho_6WO_{12} (space group R-3 (no. 148)) (Diot et al. 2000). $Y_6ReO_{14-\delta}$ is reported to crystallize in the Fm3m space group (no. 225) with a lattice size parameter of a = 10.0477(1) Å. This structure is described as a 2 x 2 x 2 superstructure of the fluorite structure with Y and Re coordinated with eight oxygen positions, which are not all occupied (Ehrenberg et al. 2004).

Due to the reported problems in refining all tungsten positions, it was found to be of interest to confirm the reported results with other diffraction techniques. Electrons interact more strongly with materials than x-rays and neutrons and are therefore more suited to study low intensity scattering (such as that of the 4d- and 24f positions). Thus electron diffraction techniques were chosen to confirm the structure and the positions of the "missing" tungsten ions.

Table 3.1: Position refinement of 2.8 •$La_2O_3WO_3$ in space group F-43m (no.216) (Magrasó et al. 2009).

Atom	Position (Wyckoff)	Coordinates	Occupancy
La	4a	0, 0, 0	1
La	24g	-0.004(6), ¼, ¼	0.928
W	4b	½, ½, ½	1
W	4d	¾, ¾, ¾	0.06(1)
W	24f	0.168(9), 0 , 0	0.02(2)
O	16e	0.1376(8), 0.1376(8), 0.1376(8)	1
O	16e	0.8677(8), 0.8677(8), 0.8677(8)	1
O	16e	0.4005(6), 0.4005(6), 0.4005(6)	0.65(3)
O	16e	0.5995(6), 0.5995(6), 0.5995(6)	0.65(3)

3.2 Synthesis of 2.8 • La$_2$O$_3$ – WO$_3$

Samples were prepared by A. Magrasó by freeze drying as reported elsewhere (Magrasó et al. 2009). Stoichiometric amounts of La$_2$O$_3$ (99.99 % Aldrich) and WO$_2$ (99.9 % Fluka) were dissolved in a diluted nitric acid solution and an ammonium hydroxide solution respectively. A complexing agent (Ethulenediamineteraacetic (EDTA) (99.7 % Aldrich)) was added to each of the solutions in a 1:1- metal:ligand mole ratio. Then the pH was adjusted between 7 and 8. The solutions were then mixed to obtain a transparent liquid without any visible precipitations. Droplets of this solution were flash- frozen in liquid nitrogen to retain the cation homogeneity and then freeze- dried (HeteroLyolab) for 3 days. The result was an amorphous precursor which was immediately heat treated at 300 ℃ (15 min) to avoid any rehydration. The powder was then heated at 600 ℃ for 2- 4 hours until a white powder was obtained. This was done to decompose and remove any residual organic substances. The powder was first heated at 1000 ℃ for 2 hours, cold pressed at 100MPa and subsequently sintered at 1500 ℃ for 2 hours in order to obtain a dense specimen.

3.3 Results - An investigation of 2.8 • La$_2$O$_3$ – WO$_3$ by TEM

3.3.1 Bravais lattice

Selected area diffraction patterns of the [100]-, see figure 3.1, [110]- and [111]-, see figure 3.2, zone axes were investigated to determine the Bravais lattice of the crystal structure. All SAD patterns were indexed in agreement with a primitive cubic Bravais lattice with a lattice size parameter of a = 11.1868(3) Å, determined by XRD/ NPD (Magrasó et al. 2009). Observed d- values of the SAD patterns have been listed in table 3.2 along with calculated d- values. The observed intensities of the reflections have been labeled; very strong (vs), strong (s) and diffuse (d).

Table 3.2: Measured SAD d- values compared to calculated d- values. The intensity of the observed reflections in SAD are denoted; very strong (vs), strong (s) and diffuse (d).

HKL	d- calculated [Å]	d- observed [Å]	RMS	Deviation [%]
100 (d)	11.18680	11.25	± 0.05	0.6
110 (d)	7.91026	7.94	± 0.05	0.4
111 (s)	6.45870	6.51	± 0.09	0.8
200 (s)	5.59340	5.59	± 0.06	0.06
210 (d)	5.00289	5.0	± 0.1	0.06
211 (d)	4.56699	4.62	± 0.07	1.2
220 (s)	3.95513	3.97	± 0.02	0.4
300 (d)	3.72893	3.75	± 0.02	0.6
311 (s)	3.37295	3.35	± 0.03	0.7
222 (s)	3.22935	3.25	± 0.05	0.6
321 (d)	2.98980	3.03	± 0.03	1.3
400 (vs)	2.79670	2.81	± 0.02	0.5
330 (d)	2.63675	2.64	± 0.01	0.1
440 (vs)	1.97757	1.979	± 0.009	0.07

Figure 3.1 shows that the diffuse reflections might be overlooked if the exposure time of the film is not long enough. The SAD patterns of the [100] projection shown in figure 3.1 were obtained at different exposure times. In the pattern with a short exposure time, the low index reflections are distinguishable and the intensities of the diffuse reflections are weak. At a higher exposure time, low index reflections are not distinguishable due to the saturation of the photographic film but the intensities and of the diffuse reflections are clearly distinguishable from the background. There are diffuse reflections which are only

distinguishable in a pattern of a long exposure time. The diffuse reflections are of type 0hh, h = 2n + 1.

The strong and very strong (not diffuse) reflections in the SAD patterns were found to be consistent with a face centered cubic Bravais lattice. The selection rules are (Hahn 1983):

hkl: h + k, h + l, k + l = 2n
0kl: k, l = 2n
hhl: h + l = 2n
h00: h = 2n
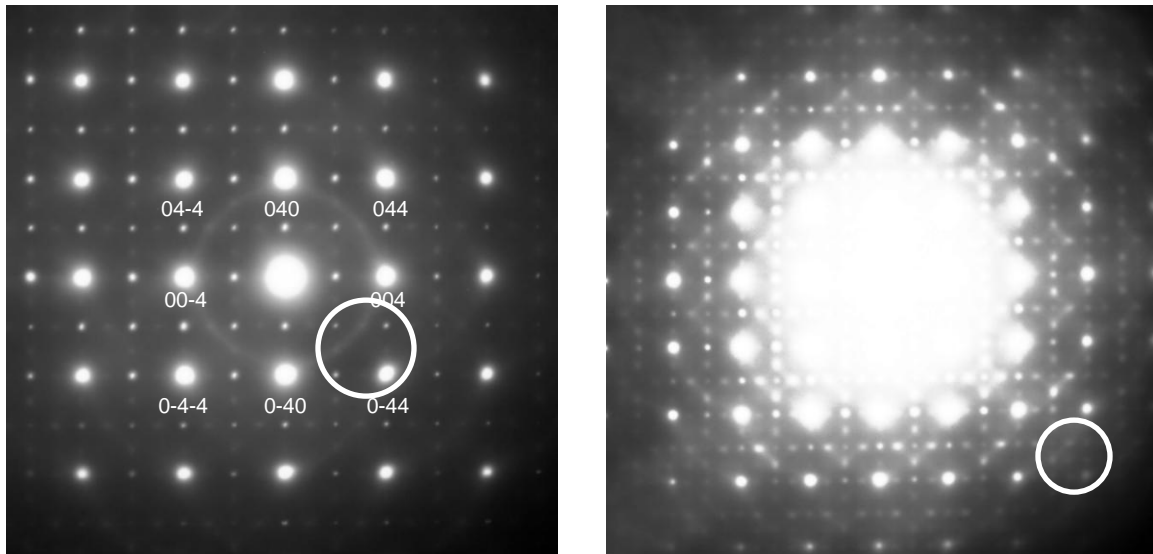
Figure 3.1: SAD patterns of the [100] projection obtained at different exposure times. In the pattern with a short exposure time (left), the low index reflections are distinguishable and the intensities of the diffuse reflections are weak. The absence of a diffuse type of reflection is marked by a circle. At a higher exposure time (right), low index reflections are not distinguishable but the diffuse reflections are clearly distinguishable from the background. There are diffuse reflections which are only distinguishable in a pattern of a long exposure time. The circle marks one of these diffuse reflections of type 0hh , h = 2n + 1 (right). Different magnifications were chosen because of saturation of low index reflections at high exposure times.
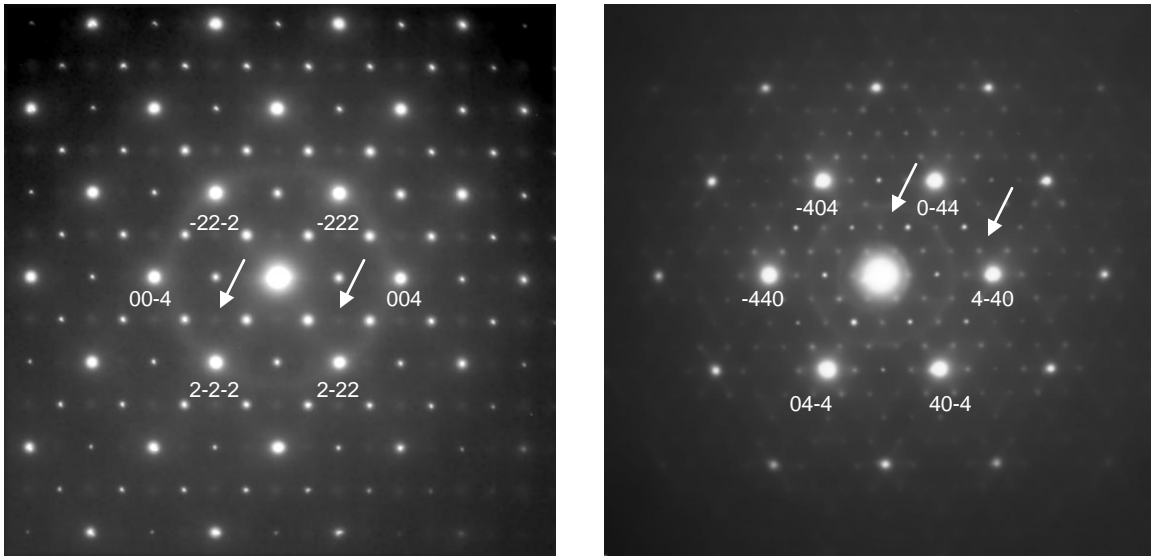
Figure 3.2: SAD patterns of the [110] - (left) and [111] (right) projections. Diffuse reflections can be observed between the stronger reflections and are indicated by arrows.

The diffuse reflections observed in all zone axis patterns did not correspond to a face centered cubic Bravais lattice. To further investigate these diffuse reflections, SAD tilt series were obtained. Three such tilt series were obtained by tilting of an axis in of the [100] - , [110] - and [111] zone axis patterns. Figure 3.3 shows two SAD patterns from the [100] tilt series separated by approximately 4 – 5°. The 002- and 012- type reflections do not diminish in intensity. The diffuse reflections increase in intensity by increasing tilt angle away from the [100] pattern. By these tilt series, several properties of the SAD pattern reflections were discovered:

- The diffuse reflections increased in intensity once the beam was tilted away from the zone axis.
- The 012- and 112 type reflections formed an arc in reciprocal space.
- Strong reflections diminished rapidly in intensity when the SAD patterns were tilted off zone axis.
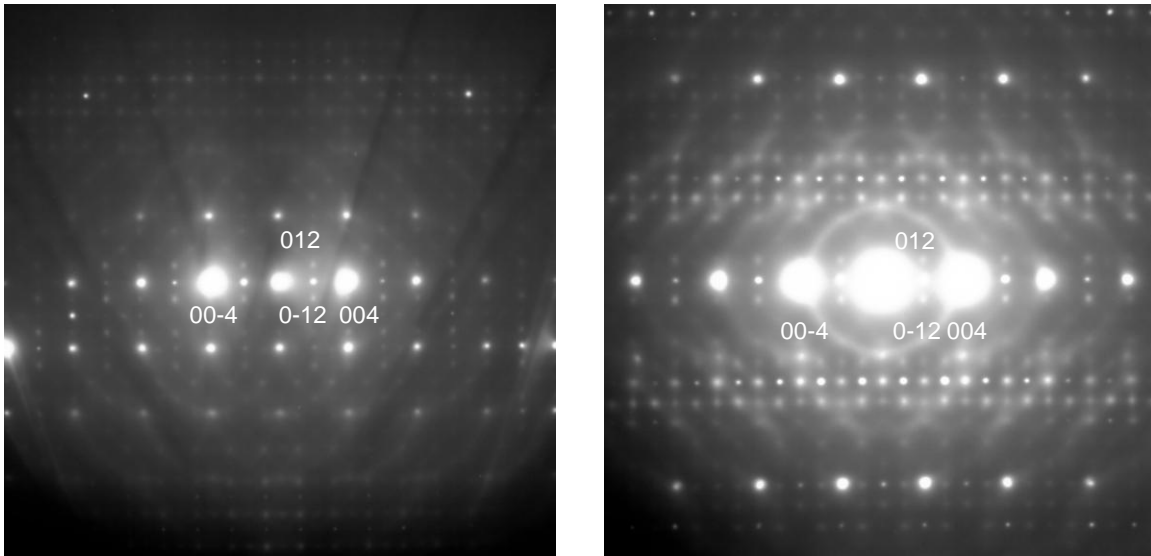
Figure 3.3: SAD patterns from the [100] tilt series separated by approximately 4 – 5°. The 002- and 012- type reflections do not diminish in intensity. The diffuse reflections increase in intensity by increasing tilt angle away from the [100] pattern (left to right).

3.3.2 Determination of point group

Whole-pattern (WP) symmetries of the [100], [110] and [111] projections were deduced to determine the crystallographic point group of the specimen.

In both CBED patterns of the [100] projection, four mirror planes separated by 45 degrees were observed, as seen in figure 3.4. This is referred to as 4mm WP and BF projection symmetry respectively. Only three point groups exhibit this WP symmetry: 4mm, 4/mmm and m3m. In both CBED patterns of the [111] projection, three mirror planes separated by 60 degrees were observed, as seen in figure 3.5. This is referred to as 3m WP and BF projection symmetry respectively. Four point groups give rise to this WP and BF symmetry: 3m, -3m, -43m and m3m. In both CBED patterns of the [110] projection, two mirror planes separated by 90 degrees were observed, as seen in figure 3.6. This is referred to as 2mm WP and BF projection symmetry respectively. This WP symmetry can be caused one of these nine point groups: mm2, mmm, m3, m3m, 4/mmm, 6m2, 6/mmm, -42m and -43m. Only a crystal structure with point group m3m exhibits these three WP symmetries. Observed WP and BF symmetries along with possible diffraction and point groups are listed in table 3.3.

Table 3.3: The deduction of the point group is based on the observed WP symmetries All WP symmetries could only be exhibited by the m3m point group.

Zone axis	WP symmetry	BF symmetry	Possible diffraction groups	Possible point groups
[100]	4mm	4mm (projection)	4mm	4mm
			4mm1$_R$	4/mmm, **m3m**
[110]	2mm	2mm (projection)	2mm	mm2, -6m2
			2mm1$_R$	mmm, 4/mmm, 6/mmm, m3, **m3m**
			4$_R$mm$_R$	-42m, -43m
[111]	3m	3m	3m	3m, -43m
			6$_R$mm$_R$	-3m, **m3m**

Figure 3.4: CBED patterns of the [100] projection. Four mirror planes separated by 45 degrees were observed in the pattern obtained at a small camera length (left). This is referred to as 4mm WP symmetry. Four mirror planes separated by 45 degrees were observed in the pattern obtained at a large camera length (right). This is referred to as 4mm BF projection symmetry.
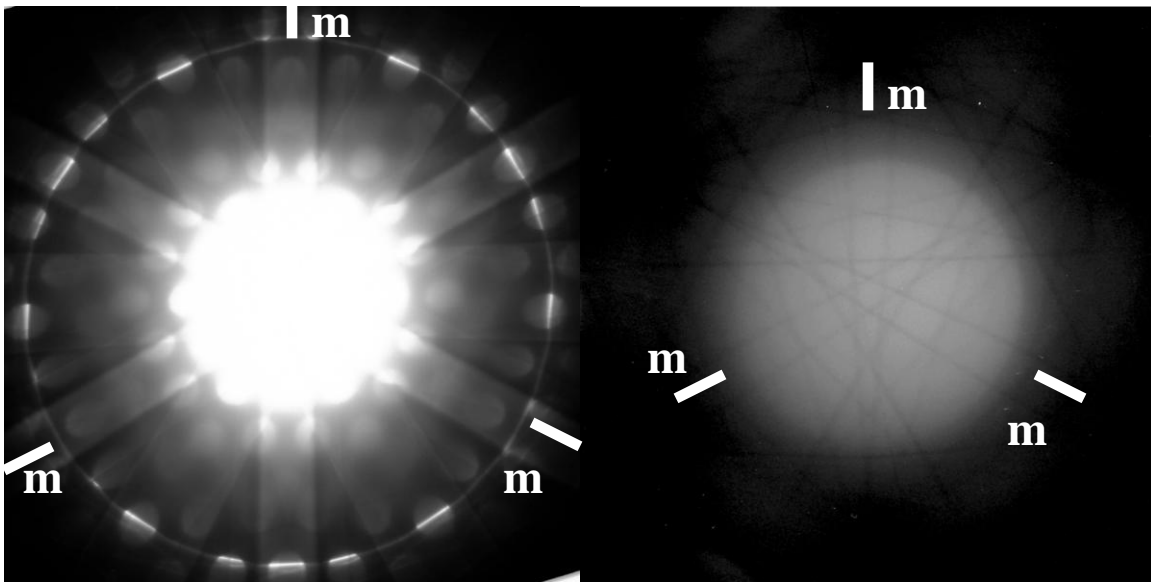
Figure 3.5: CBED patterns of the [111] projection. Three mirror planes separated by 60 degrees were observed in the pattern obtained at a small camera length (left). This is referred to as 3m WP symmetry. Three mirror planes separated by 60 degrees were observed in the pattern obtained at a large camera length (right). This is referred to as 3m BF symmetry.
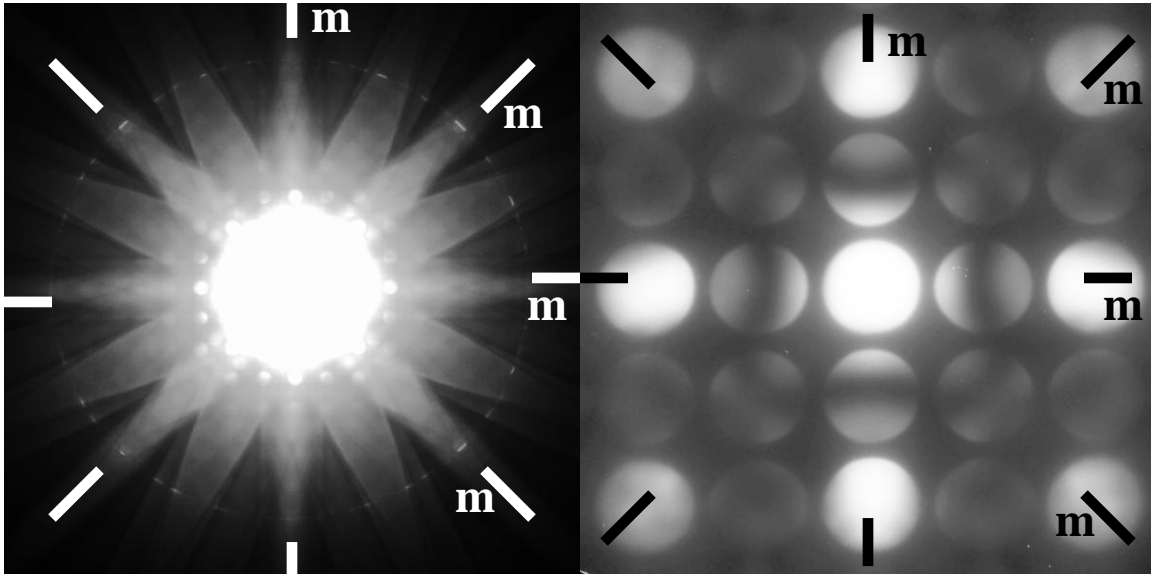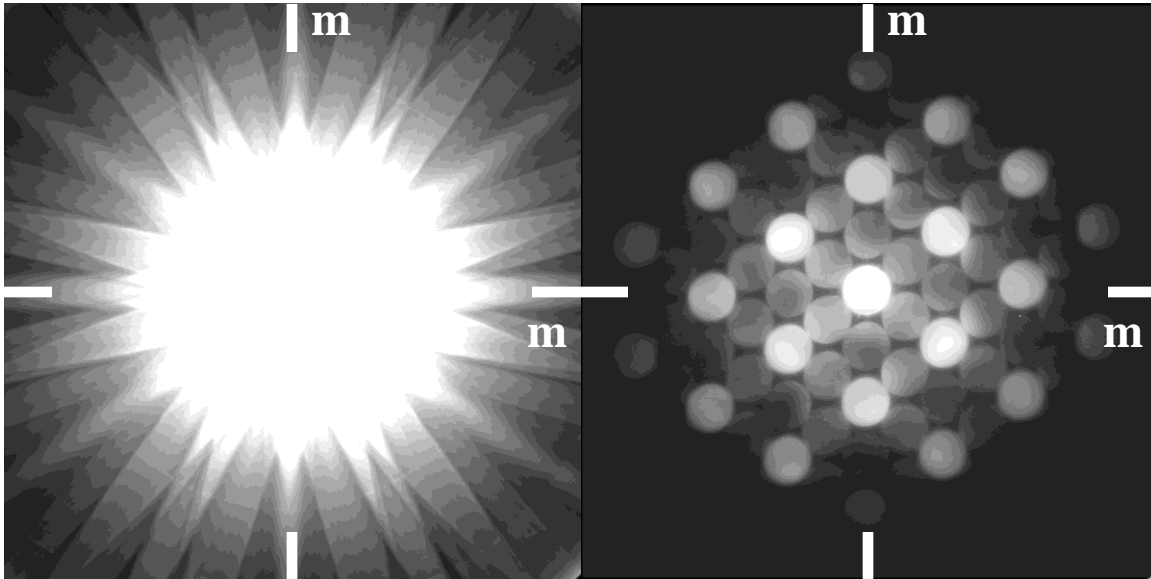
Figure 3.6: CBED patterns of the [110] projection. Two mirror planes separated by 90 degrees were observed in the pattern obtained at a small camera length (left). This is referred to as 2mm WP symmetry. Two mirror planes separated by 90 degrees were observed in the pattern obtained at a large camera length (right). This is referred to as 2mm BF projection symmetry.

3.3.3 Space group

A single crystal was investigated. The ZOLZ (zero order Laue zone) of the [100] projection seemed to contain dynamical extinction lines, called Gjønnes- Moodie B_2-lines, in the 002, 00-2, 020 and 0-20 discs, see figure 3.7. These reflections are therefore kinematically forbidden due to a 4_1 or 4_3 screw axis (Gjonnes and Moodie 1965; Hahn 1983; Tanaka et al. 1983, 2). This is in disagreement with the results reported for XRD and NPD (Magrasó et al. 2009). This result is also in disagreement with that the intensity of the 002 -type reflections did not change when the SAD patterns were tilted of the [100] zone axis. This is expected to occur for reflections which are observed due to dynamical rather than Bragg scattering (Williams and Carter 1996). The crystal can bee seen in figure 3.8. The amorphous edge observed in the image is most likely caused by mechanical damage from the ion beam during ion milling.

These GM lines have been observed in all crystals and all samples where the [100] projection has been investigated. That indicates that this result is not coincidental.

EDS investigations uncovered no significant compositional variations in different grains or within a single grain of a specimen, se figure 3.9 and table 3.4. The La/W mole ratio was in congruence with the nominal mole ratio of 5.6 and the mole ratio of 5.71 observed by electron probe micro analysis (EPMA) (Magrasó et al. 2009). Composition was calculated by the Noran System Six software using the Cliff- Lorimer correction method without absorption. The cupper detected by EDS is probably caused by sputtering of the Cu support ring during ion milling, see figure 3.9.
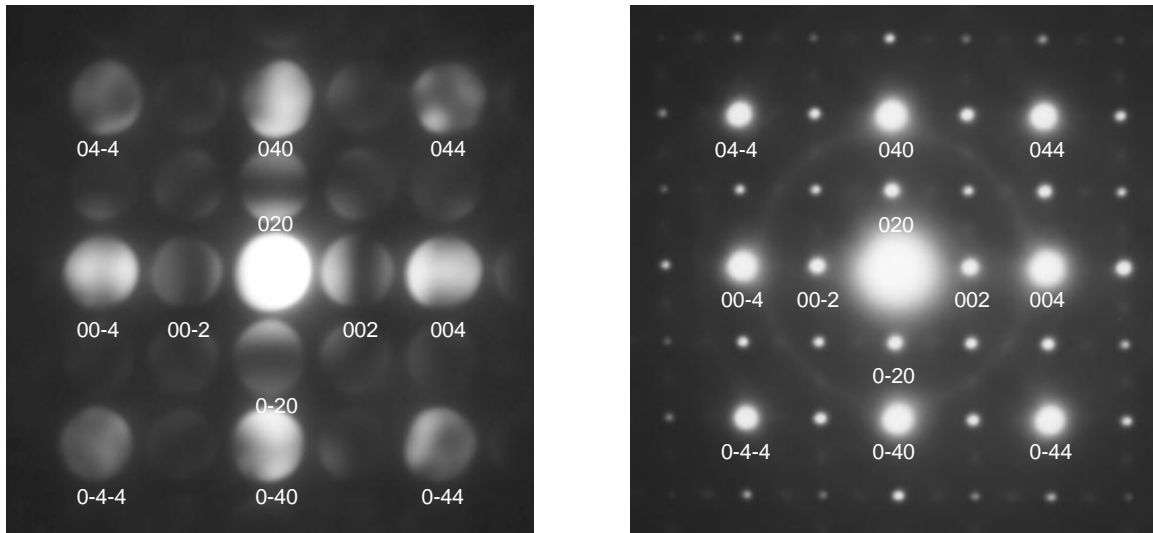
Figure 3.7: CBED pattern of the ZOLZ exhibiting what appears to be B_2 GM lines in the 002, 00-2, 020 and 0-20 reflections (left).
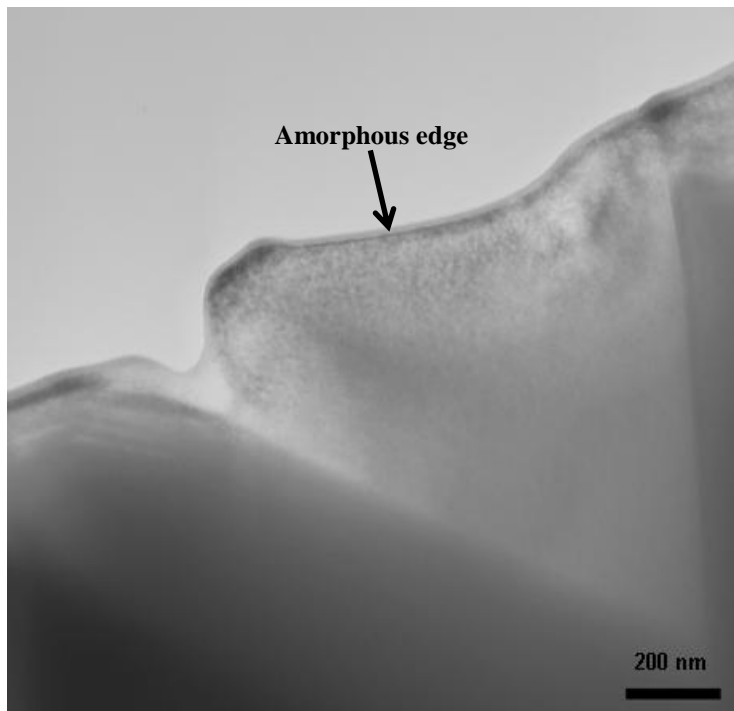
Figure 3.8: TEM image of the crystal at [100] beam incidence. The amorphous edge is most likely caused by damage from the ion beam by ion milling.
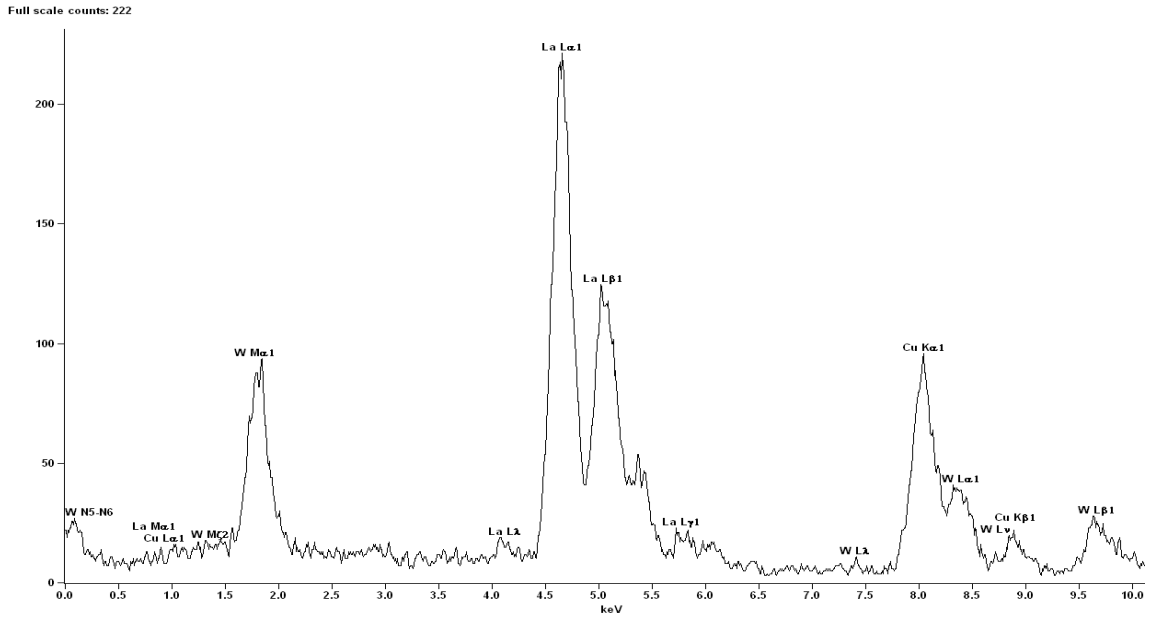
Figure 3.9: EDS spectrum of the lanthanum tungstate crystal.

Table 3.4: Composition of the single crystal from EDS data.

Element, line	Composition [Atom %]	Error [Atom %]
La, L	**85.94**	**± 4.22**
W, L	**14.06**	**± 1.53**
La, L	83.44	± 4.58
W, L	16.56	± 1.70
La, L	83.88	± 2.15
W, L	16.12	± 1.48

3.4 Discussion

3.4.1 Strong reflections and CBED

Lanthanum tungstate with a nominal mole ratio of 2.8:1 La_2O_3- WO_3 has been investigated by selected area- and convergent beam electron diffraction in order to determine its crystal structure and space group. The reflection conditions for the strong reflections observed in the SAD patterns indicate a face centered cubic Bravais lattice. The point group deduced by the symmetry of the [100], [110] and [111] CBED zone axis patterns is m3m. The dynamical extinctions observed in the 002 type reflection discs of the [100] projection indicate the presence of a 4_1 or 4_3 screw axis. F-43m (no. 216) is the reported space group for the crystal structure refined from x- ray- and neutron diffraction data (Magrasó et al. 2009).

The presence of a 4_1 or a 4_3 screw axis, the m3m point group and the conditions for the strong reflections indicate the Fd3m space group. The convergent beam information is gathered from a small area of the sample. The symmetry of this area might be described by this space group. The 002 reflection might still be caused by Bragg scattering due to local structural disorder. This is in agreement with experimental results if the contribution of this reflection is so weak that it is masked by the dominating screw axis in the [100] CBED pattern. If this is the case, the symmetry should rather be referred to as pseudo Fd3m symmetry.

A larger area is investigated in SAD than in CBED, see figure 1.5. The selected area patterns include a relatively strong intensity of the 002 type reflections. The intensity of these reflections does not change when the sample is tilted of a zone axis. A change in intensity would be expected if a reflection is kinematically forbidden and was caused by purely dynamical scattering. This indicates a breakdown in symmetry which allows 002 type reflections to a higher degree than in the area investigated by CBED. This breakdown might be explained by that within the area investigated by SAD, there is structural disorder which destroys the diamond glide plane symmetry of Fd3m. This would be consistent with space group Fm3m (no. 225). Disorder might also break down the whole pattern symmetry for the [100] projection from 4mm to 2mm. Such a decrease in symmetry would be consistent with both the m3m- and the -43m point group, see table 3.5. The WP symmetry of the [100] projection in the present CBED patterns might

71

actually be 2mm, but the intensity of this contribution is too low to be distinguished in the obtained patterns.

Table 3.5: The deduction of both the m3m and the -43m point group, if the WP symmetry of the [100] projection is 2mm.

Zone axis	WP symmetry	BF symmetry	Possible diffraction groups	Possible point groups
[100]	2mm	4mm (proj.)	2mm	mm2, -6m2
			$2mm1_R$	mmm, 4/mmm, 6/mmm, m3, **m3m**
			4_Rmm_R	
				-42m, **-43m**
[110]	2mm	2mm (proj.)	2mm	mm2, -6m2
			$2mm1_R$	mmm, 4/mmm, 6/mmm, m3, **m3m**
			4_Rmm_R	-42m, **-43m**
[111]	3m	3m	3m	3m, **-43m**
			6_Rmm_R	-3m, **m3m**

3.4.2 Diffuse reflections

The SAD patterns included diffuse reflections which indicate a primitive Bravais lattice. These reflections might be explained by a decrease in symmetry, which might be caused by structural disorder. The diffuse arcs observed for the 012 and 112 type reflections might also be caused by disorder. Suzuki et al. have examined SAD patterns obtained from samples of different compositions in the ZrO_2- Y_2O_3 system in a series of three papers. Diffuse reflections and arcs were observed in the SAD patterns similar to those observed in the present study, and were accredited to oxygen ion displacements of the proposed modulated structure (Suzuki et al. 1985; Suzuki et al. 1987, 1; Suzuki et al. 1987, 2). Randal et al. have studied the disorder-order perovskite $Pb(In_{0.5}Nb_{0.5})O_3$. Diffuse superstructure reflections similar to those of observed in current SAD patterns was observed. These reflections were accredited to ~20- 30 nm domains and ordered B-

site sub-lattice modulating dipole displacements of the ions on the A- site sub-lattice (Randall et al. 1988). This indicates that diffuse reflections observed in current SAD patterns might be caused by disorder. A primitive Bravais lattice is in disagreement with space group F-43m. Electrons are much more sensitive to small structural variations than XRD and NPD. The low intensity of these reflections suggests that they are below the sensitivity limit of x- ray and neutron diffraction. The structure might therefore be described in space group Pm3m (no.221) or P-43m (no.215).

3.4.3 Composition

A decrease in symmetry in larger areas might be explained by domains of different phases or compositions. Energy dispersive x-ray spectroscopy was used to investigate any compositional changes within the area investigated by SAD. No difference in composition was found. This is in agreement with reported XRD and microprobe results which only detected a single phase (Magrasó et al. 2009). There might still be compositional variations within the analyzed area which are undetectable by EDS, XRD and EMPA. This might be caused by small size of compositional domains (below spatial resolution of EDS) or a by small changes in the chemical composition (below sensitivity of EDS).

3.4.5 Description of the structure

The structural description of 2.8:1 La_2O_3- WO_3 is a matter of which order of magnitude it is described. At a small scale, the structure seems to be highly pseudo- symmetric and might be described by the space group Fd3m (no. 227). At a slightly larger scale the symmetry decreases and the structure might be described by the space group P-43m (no. 215) or Pm3m (no.221). P-43m is a subgroup of F-43m which is a subgroup of Fd3m. Pm3m is a subgroup of Fm3m (Hahn 1983). These crystallographic relations do not contradict a decrease in symmetry. The reason for a breakdown in symmetry might by compositional variations which are too small to be detected by EDS. This breakdown might also be caused by structural variations which are too small to be identified by SAD. Such variations might be general disorder or nano- scale structured artifacts.

3.4.5 Consistency

X-ray- and neutron diffraction data originate from a bulk sample, while electron diffraction data originate from small areas. If a sample is perfectly homogenous and perfectly ordered, all methods should give rise to the same result. This is not the case in the present investigation. The effect of deviations from an ideal structure might manifest itself differently at different orders of magnitude. The sensitivity to different structural features of the different techniques might also result in deviation of results. This fact must be taken into consideration when a description of the structure is proposed.

SAD patterns and CBED patterns deviate from each other and the structure suggested by XRD/ NPD. The $La_{26.5}W_{4.7(4)}O_{52.8(9)}$ unit cell composition and refinement proposed by NPD and XRD (Magrasó et al. 2009) therefore might be regarded as an average description of the crystal structure. The reason for this inconsistency has yet to be uncovered.

3.5 Conclusions

- CBED and the strong reflections observed by SAD patterns indicate a quasi-Fd3m symmetry at a small scale.

- Diffuse reflections observed by SAD indicate a primitive Bravais lattice and a breakdown of the quasi- Fd3m symmetry at a larger scale than investigated by CBED.

- The F-43m space group determined by XRD and NPD is in disagreement with SAD and CBED patterns obtained during this investigation.

- No compositional variations have been detected by EDS.

3.5.1 Suggestions for further work

- Investigate the ordering of the structure and three-dimensional elemental distribution at an atomic scale. Proposed techniques are high resolution TEM imaging (HREM) and high angular annular dark field (HAADF) scanning transmission electron microscopy (STEM).

- Investigate the effect of temperature on the structure in a water atmosphere. Proposed technique is environmental-HREM.

- Investigate the composition and electronic structure. Proposed technique is electron energy loss spectroscopy (EELS).

- Perform refinement of XRD and NPD data to confirm compatibility with a primitive Bravais lattice.

Appendix A

Acronyms

Acronym	Full name
BF	Bright Field
BSE	Back Scattered Electrons
CBED	Convergent Beam Electron Diffraction
DP	Diffraction Pattern
EELS	Electron Energy Loss Spectroscopy
ED	Electron Diffraction
EDS	Energy Dispersive Spectroscopy
EPMA	Electron Probe Micro Analysis
FEG	Field Emission Gun
FOLZ	First Order Laue Zone
GM	Gjønnes- Moodie
HAADF	High Angular Annular Dark Field
HOLZ	Higher Order Laue Zones
JEOL	Japanese Electron Optics Laboratory Co., Ltd
JEM	Japanese Electron Microscope
NPD	Neutron Powder Diffraction
NSS	Noran System Six
SAD	Selected Area Diffraction
S/cm	Siemens/cm
SE	Secondary Electrons
SEM	Scanning Electron Microscope

SOFC	Solid Oxide Fuel Cell
SOLZ	Second Order Laue Zone
STEM	Scanning Transmission Electron Microscope
TEM	Transmission Electron Microscope
Wt %	Weight Percent
WP	Whole Pattern
XRD	X-ray Diffraction
ZOLZ	Zero Order Laue Zone
Å	Ångström, 10^{-10} m

Appendix B

Symbols

Symbol	Description
α	Convergence semi angle
a	Lattice size parameter [Å]
A_2	Dynamical extinction line in a CBED reflection disc, caused by two dimensional interactions, which indicate a glide plane
A_3	Dynamical extinction line in a CBED reflection disc, caused by three-dimensional interactions, which indicate a glide plane
B_2	Dynamical extinction line in a CBED reflection disc, caused by two dimensional interactions, which indicate a screw axis.
B_3	Dynamical extinction line in a CBED reflection disc, caused by three-dimensional interactions, which indicate a screw axis.
C_i	Mass concentration of element i.
d	Lattice plane distance [Å]
hkl	Miller indices
I_i	Observed intensity of characteristic x- ray radiation originating from element i.
K	Camera constant
k_{ij}	Cliff- Lorimer k- factor
$K\alpha_1$	Characteristic x- ray radiation
λ	Wavelength of radiation
n	An integer
L	Camera length
R and r	Measured distance from the central beam to a Bragg reflection in electron diffraction patterns.

r_1	Measured radius of reflection disc in CBED patterns
θ_B	Bragg scattering angle
Z	Mean atomic number of a compound

References

Aeasar, A. (2008). "Material Safety Data Sheet."   Retrieved 05.05.09, 2009, from http://www.alfa.com/content/msds/USA/11309.pdf.

Brixner, L. H. (1964). "Preparation and Properties of the $Ln_2Ti_2O_7$-Type Rare Earth Titanate." <u>Inorg. Chem.</u> **3**(7): 1065-1067.

Buxton, B. F. et al. (1976). "The Symmetry of Electron Diffraction Zone Axis Patterns." <u>Philosophical Transactions of the Royal Society of London. Series A, Mathematical and Physical Sciences</u> **281**(1301): 171-194.

Chakoumakos, B. C. (1984). "Systematics of the pyrochlore structure type, ideal A2B2X6Y." <u>Journal of Solid State Chemistry</u> **53**(1): 120-129.

Diot, N. et al. (2000). "X-ray powder diffraction data a dn Rietveld refinemnt for Ln6WO12 (Ln=Y, Ho)." <u>Powder Diffraction</u> **15**(4): 220-226.

Ehrenberg, H. et al. (2004). "Yttrium rhenium oxide, $Y_7ReO_{14-\delta}$: a cubic fluorite superstructure." <u>Solid State Sciences</u> **6**(3): 247-250.

Fjeld, H. et al. (2008). "Proton and oxide ion conductivity in grain boundaries and grain interior of Ca-doped $Er_2Ti_2O_7$ with Si-impurities." <u>Solid State Ionics</u> **179**(33-34): 1849-1853.

Gjonnes, J. and A. F. Moodie (1965). "Extinction conditions in the dynamic theory of electron diffraction." <u>Acta Crystallographica</u> **19**(1): 65-67.

Hahn, T. (1983). <u>International Tables for Crystallography,</u> Volume A: Space-Group Symmetry, D. Reidel Publishing Company.

Haugsrud, R. (2007). "Defects and transport properties in Ln_6WO_{12} (Ln = La, Nd, Gd, Er)." <u>Solid State Ionics</u> **178**(7-10): 555-560.

Haugsrud, R. and C. Kjølseth (2008). "Effects of protons and acceptor substitution on the electrical conductivity of La_6WO_{12}." <u>Journal of Physics and Chemistry of Solids</u> **69**(7): 1758-1765.

Knop, O. et al. (1969). "Pyrochlores. V. Thermoanalytic, x-ray, neutron, infrared, and dielectric studies of $A_2Ti_2O_7$ titanates." <u>Canadian Journal of Chemistry</u> **47**(6): 971-90.

Knop, O. et al. (1965). "Determination of the crystal structure of erbium titanate, Er2Ti2O7, by x-ray and neutron diffracton." <u>Can. J. Can. Chem.</u> **43**(10): 2812-26.

Kramer, S. et al. (1994). "Conduction in titanate pyrochlores: role of dopants." Solid State Ionics **72**(Part 2): 59-66.

Shcherbakova, L. G. et al. (1979). "Lanthanide Titanates." Russian Chemical Reviews **48**(3): 228-242.

Lau, G. C. et al. (2006). "Stuffed rare earth pyrochlore solid solutions." Journal of Solid State Chemistry **179**(10): 3126-3135.

Lian, J. et al. (2003). "Radiation-induced amorphization of rare-earth titanate pyrochlores." Physical Review B **68**(13): 134107, 1 - 9.

Magrasó, A. et al. (2009). "Crystal structure determination and charaterization of lanthanum tungstate prepared by freeze-drying." Submitted

Minervini, L. et al. (2000). "Disorder in Pyrochlore Oxides." Journal of the American Ceramic Society **83**(8): 1873-1878.

Minervini, L. et al. (2002). "The oxygen positional parameter in pyrochlores and its dependence on disorder." Philosophical Magazine A **82**(1): 123 - 135.

Müller, U. (2006). "Remarks on Wychoff positions " International Tables for Crystallography 1st online ed. Retrieved 31.05.2009, Volume A1: Symmetry relations between space groups, from http://it.iucr.org/A1a/ch1o3v0001/ch1o3.pdf.

Norby, T. (1998). High Temperature Proton Conductors. Hydrogen Power: Theoretical and Engineering Solutions. T. O. Saetre, Kluwer Academic Publishers**:** 603- 608.

Olsen, A. (2008). The Theory and Practice of Analytical Electron Microscopy in Matreials Sience. Oslo, Department of Physics, Univeristy of Oslo, Norway

Pirzada, M. et al. (2003). "Incorporation of divalent ions in $A_2B_2O_7$ pyrochlores." Solid State Ionics **161**(1-2): 81-91.

Pirzada, M. et al. (2001). "Oxygen migration in $A_2B_2O_7$ pyrochlores." Solid State Ionics **140**(3-4): 201-208.

Randall, C. A. et al. (1988). "TEM study of the disorder-order perovskite, $Pb(In_{1/2}Nb_{1/2})O_3$." Journal of Materials Science **23**(10): 3678-3682.

Shlyakhtina, A. V. et al. (2007). "Order-disorder phase transitions and high-temperature oxide ion conductivity of $Er_{2+x}Ti_{2-x}O_{7-\delta}$ (x = 0, 0.096)." Materials Research Bulletin **42**(4): 742-752.

Stambouli, A. B. and E. Traversa (2002). "Solid oxide fuel cells (SOFCs): a review of an environmentally clean and efficient source of energy." Renewable and Sustainable Energy Reviews **6**(5): 433-455.

Steeds, J. W. and R. Vincent (1983). "Use of high-symmetry zone axes in electron diffraction in determining crystal point and space groups." Journal of Applied Crystallography **16**(3): 317-324.

Straumanis, M. E. et al. (1961). "Perfection of the Lattice of Dislocation-Free Silicon, Studied by the Lattice-Constant and Density Method." Journal of Applied Physics **32**(7): 1382-1384.

Subramanian, M. A. et al. (1983). "Oxide pyrochlores -- A review." Progress in Solid State Chemistry **15**(2): 55-143.

Subramanian, M. A. and A.W Sleight, Ed. (1993). Rare Earth Pyrochlores. Handbook on the Physics and Chemistry of Rare Earths. Amsterdam, Elsevier Science Publishers B.V.

Suzuki, S. et al. (1985). "Structural Studies on ZrO_2-Y_2O_3 System by Electron Diffraction and Electron Microscopy I." Japanese Journal of Applied Physics **24**(4).

Suzuki, S. et al. (1987, 1)."Structural studies on the ZrO_2-Y_2O_3 system by electron diffraction and electron microscopy. II." Journal of Physics C: Solid State Physics(20): 2963.

Suzuki, S. et al. (1987, 2). "Structural Studies on the ZrO_2-Y_2O_3 System by Electron Diffraction and Electron Microscopy III." Japanese Journal of Applied Physics **26**(12).

Tabira, Y. et al. (2000). "Systematic Structural Change in Selected Rare Earth Oxide Pyrochlores as Determined by Wide-Angle CBED and a Comparison with the Results of Atomistic Computer Simulation." Journal of Solid State Chemistry **153**(1): 16-25.

Tanaka, M. et al. (1983, 1). "Point-group determination by convergent-beam electron diffraction." Acta Crystallographica Section A **39**(3): 357-368.

Tanaka, M. et al. (1983, 2). "Space-group determination by dynamic extinction in convergent-beam electron diffraction." Acta Crystallographica Section A **39**(6): 825-837.

Tuller, H. L. (1994). Defects and Disorder in Crystalline and Amorphous Solids. C. R. A. Catlow, Kluwer**:** 189.

Vigen, C. C. and O.-A. Ertzied (2007). "MEF3100 Prosjekt $Er_{1,96}Ca_{0,04}Ti_2O_7$".

Wilde, P. J. and C. R. A. Catlow (1998). "Defects and diffusion in pyrochlore structured oxides." Solid State Ionics **112**(3-4): 173-183.

Williams, D. B. and C. B. Carter (1996). Transmission Electron Microscopy, II Diffraction. New York, Plenum Press.